Computational Investigations of Vortex Dynamics and Dynamic Stall of Pitching Airfoils at High Reynolds Number

by

Hao Wang

A thesis presented to Lakehead University

in fulfilment of the

thesis requirement for the degree of

Master of Applied Science in

Mechanical and Mechatronics Engineering

Thunder Bay, Ontario, Canada, 2025

I hereby declare that I am the sole author of this thesis.

I authorize Lakehead University to lend this thesis to other institutions or individuals for the purpose of scholarly research.

(Insert signature)

I further authorize Lakehead University to reproduce this thesis by photocopying or by other means, in total or in part, at the request of other institutions or individuals for the purpose of scholarly research.

(insert signature)

Lakehead University requires the signatures of all persons using or photocopying this thesis. Please sign below and give address and date.

Abstract

This study employs high-fidelity Detached Eddy Simulations (DES) and modal decompositions to elucidate dynamic stall mechanisms on a pitching NACA 0018 airfoil at $Re = 160000$. *Proper Orthogonal Decomposition (POD) isolates leading-edge separation bubbles, shear-layer instabilities, and wake vortices by energy content, while Dynamic Mode Decomposition (DMD) and multiresolution DMD (mrDMD) reveal mode-specific growth/decay rates and frequencies across reduced frequencies* ($k = 0.1, 0.2, 0.3$) *and amplitudes* ($\alpha = 15 - 30°$). *DMD captures key events—LSB bursting, LEV formation, and DSV convection—with global modes sufficient for most cases, whereas mrDMD improves reconstruction only under deep stall* ($k = 0.1, \alpha = 30°$) *These findings provide a low-order framework for predicting unsteady loads and guiding stall mitigation strategies.*

Acknowledgements

First, I would like to express my deepest gratitude to my supervisor, **Dr. Muhammad Saif Ullah Khalid**, for his patient guidance, invaluable feedback, and unwavering support throughout every stage of this research.

I am also grateful to the members of my thesis committee—Dr. Ahmed Elshaer and Dr. Ali Tarokh for their insightful comments and constructive critiques, which greatly enhanced the quality of this work.

This work was funded by Discovery Grant and Alliance International (Catalyst) grant from Natural Sciences and Engineering Research Council of Canada (NSERC), and Global Research Award from MITACS, whose financial supports are gratefully acknowledged. I also thank Nature Inspired Engineering Research Lab for providing the research facilities and Lakehead University for administration assistance. Additionally, I would like to show my appreciation towards my lab mates Maham Kamran, Faisal Muhammad, Dev Nayak, Dilip Thakur, Amirhossein Fardi for the simulating conversation and emotional support.

Finally, I wish to thank my family and friends for their love, patience, and encouragement—especially Feiyu Mo, Zhaojun Wang and Cuixia Cai and my friends —without whom this journey would not have been possible.

Table of Content

List of Figures

Chapter 1

Introduction

This thesis presents a comprehensive investigation into the unsteady aerodynamics of a two-dimensional pitching NACA 0018 airfoil at a transitional Reynolds number of $160\ 000$, combining high-fidelity Detached Eddy Simulations (DES) with complementary modal decomposition techniques to elucidate both energetic and dynamical features of dynamic stall. By systematically varying reduced frequency ($k = 0.1, 0.2, 0.3$) and pitching amplitude ($\alpha = 15°, 20°, 25°, 30°$), we capture a wide range of transient flow behaviors — from mild oscillatory separation to deep stall—and quantify their influence on lift, drag, and vortex formation. Proper Orthogonal Decomposition (POD) distills the most energetic coherent structures, while Dynamic Mode Decomposition (DMD) extracts mode-specific growth/decay rates and oscillation frequencies, yielding insights into instability mechanisms. In addition, we perform multi-resolution DMD (mrDMD) on the two-dimensional data to compare its accuracy against classical DMD across the parametric space, revealing that mrDMD outperforms DMD only in the case of the lowest reduced frequency ($k = 0.1$) combined with the highest amplitude ($\alpha = 30°$). Three-dimensional reconstructions of key modal features bridge the gap between 2D analyses and real-world aerodynamic applications, laying the groundwork for advanced flow-control strategies.

Dynamic stall arises a critical issue (Hand, 2017; Le Fouest, 2022) for the self-staring performance on vertical axis wind turbines (VAWT) and other aerodynamic designs where it

undergoes rapid angular excursions beyond its static stall angle (Hill, 2009), leading to the formation of a coherent leading-edge vortex (LEV) (Kurtulus, 2015) that temporarily enhances lift before bursting and shedding, causing abrupt load fluctuations (Sudharsan, 2024). The dimensionless reduced frequency, $k = \frac{2\pi f c}{U}$, governs the ratio of pitching to convective timescales: higher k delays LEV detachment and mitigates peak load overshoots via unsteady camber effects (Honarmand, 2019), while lower k may preclude organized vortex shedding (Wang W. a., 2021). Pitching amplitude α controls the severity of stall: small amplitudes yield mild separation bubbles (Batther, 2022), whereas large amplitudes generate strong LEVs (McAlister, 1978) and pronounced hysteresis in lift and drag loops (Kurtulus, 2015). Understanding these parametric effects is critical for rotorcraft blades, flapping-wing micro-air vehicles, and vertical-axis wind turbines, where unsteady loads dictate performance limits and structural fatigue life.

To resolve the intricate flow physics at $Re = 1.6 \times 10^5$, we employ 3-Dimesional DES on an o-grid structured mesh that follows the sinusoidal pitching motion of the airfoil with the span of 0.2c. DES hybrids (Travin A. a., 2000) Reynolds-Averaged Navier–Stokes (RANS) modelling in attached boundary layers with Large-Eddy Simulation (LES) (Spalart, 2009; Madsen, 2009) of separated shear layers, offering a cost-effective yet high-fidelity (Shur, 2008; Travin A. K., 2006) framework for unsteady separation and vortex dynamics (Kozelkov, 2016). Rigorous 3-Dimensional mesh and time-step independence studies ensure numerical accuracy across all combinations of reduced frequency (k) and pitching amplitude (A). Vortex dynamics visualization techniques, Q-criterion along with force coefficients (C_L, C_D) and surface pressure

distributions are recorded over multiple oscillation cycles, enabling both phase-resolved and cycle-averaged analyses.

Inspired from sinusoidal protuberances on the flippers of the humpback whale (Fish, 1995), tubercles on the leading edge of wings of rotors and blades of turbines significantly alter their stall behavior (Hansen, 2012). In steady flows at low-to-moderate Reynolds numbers (on the order of 10^5), a wing with a tubercles leading edge can delay onset of stall (Zhao M. a., 2023) and modify the post-stall performance by generating streamwise vortices that energize the boundary layer (Zhao M. a., 2021). For example, experiments at $Re \sim 10^5$ on a cambered E216 airfoil showed that tubercles yielded higher lift coefficients (up to $\sim$ 4.5%improvement) in the pre-stall regime compared (Sreejith, 2020) to a baseline airfoil, but with a penalty in the form of slight increase in drag penalty (Zhao M. a., 2017). The primary flow mechanism involves formation of counter-rotating vortex pairs at each tubercle (He, 2023), which channel high-momentum fluid from the free stream into the near-wall region downstream of troughs (Cai, 2022). It results in a spanwise undulating separation line and the compartmentalization of separated flows into discrete "stall cells" between the peaks of tubercles (Ouro, 2018; Ahmad, 2023). The enhanced mixing and momentum transfer induced by these streamwise vortices can stabilize the laminar separation bubble and delay flow separation over the tubercled sections of the wing (Hrynuk, 2020). However, past the phase of stall the benefits of having tubercles on the leading edge of a wing diminish (Hansen, 2012). Beyond a certain angle of attack (e.g. $\alpha \approx 20^\circ$) the attached flow regions between stall cells do not extend much past mid-chord (Zhao M. a., 2017), and the overall gain in the aerodynamic lift is marginal (Badia, 2024).

Modal decomposition provides powerful, reduced-order descriptions (Wang Z. a., 2012) of complex flows. Proper Orthogonal Decomposition (POD) decomposes the velocity field into orthogonal modes (Berkooz, 1993) ranked by kinetic energy (Chatterjee, 2000), isolating dominant structures such as laminar separation bubbles (Ribeiro, 2017), shear-layer vortices, and trailing-edge instabilities (LeGresley, 2000). Dynamic Mode Decomposition (DMD) associates each spatial mode with a single complex eigenvalue (Tu, 2013): its magnitude encodes exponential growth or decay (Schmid, 2010), and its argument gives the oscillation frequency (Kutz J. N., 2016; Hemati, 2014). By applying a moving-boundary correction to account for the pitching motion, we extract physically meaningful DMD modes that characterize instability mechanisms (Mohan, 2016), including shear-layer roll-up frequencies and LEV shedding rates (Askham, 2018).

Recognizing that classical DMD may conflate modes across disparate timescales, we also implement multi-resolution DMD (mrDMD) on the two-dimensional data set. mrDMD recursively decomposes the time window into hierarchical levels (Kutz J. N., 2016), isolating slow- and fast-timescale behaviors (Dylewsky, 2019). A comparative study across all cases combination of $k - \alpha$ demonstrates that mrDMD yields lower overall modal accuracy, However, when measured by reconstruction error and frequency resolution, only for the lowest reduced frequency ($k = 0.1$) at the largest pitching amplitude ($\alpha = 30°$), mrDMD yields a better accuracy which signifies deep dynamic stall and more complex instabilities (Miotto, 2022). For all other parameter combinations, classical DMD suffice (Yang, 2022), indicating that the added complexity of mrDMD is warranted only under strongly nonlinear, low-frequency forcing.

This thesis addresses several gaps in existing literature: (1) a systematic parametric DES study at high Reynolds number spanning multiple k and α_o values; (2) dual-modal analysis using POD and DMD on the same data set; (3) integration of two- and three-dimensional modal reconstructions; and (4) the first comparative assessment of mrDMD versus DMD in unsteady aerodynamic contexts. The findings inform passive and active flow-control strategies—such as leading-edge morphing or synthetic jet actuation—to mitigate adverse stall effects.

Chapter 2

Computational Methodology

Geometry & Kinematics

In this work, standard and tubercle pitching wings are employed to model an oscillating blade of a VAWT (Hand, 2017). The primary objective here is to explore the changes in vortex dynamics that arise during the wing's motion, particularly how the leading-edge vortices (LEVs) and trailing edge vortices (TEVs) behave instantaneously (Laneville, 1986). Given that the scope of this study is centered on the analysis of these vortical structures, a relatively simple oscillatory motion is prescribed for the wing that performs pitching around an axis located at a distance of 0.25c from the leading edge. Here, c denotes the chord of the wing. Previous studies showed that a simple sinusoidal pitching motion could be used to study dynamic stall because it reproduced the essential unsteady vortex phenomena observed in and aligned with experimental results. For example, Mallik et al. (Mallik, 2020) performed hybrid RANS/LES (DDES) simulations of a NACA 0012 airfoil undergoing light dynamic stall (Wang W. a., 2021). Furthermore, researches presented studies to confirm that a single-frequency pitching motion was sufficient to produce the vortex dynamics (shear layer roll-up, vortex shedding, etc.) associated with dynamic stall.

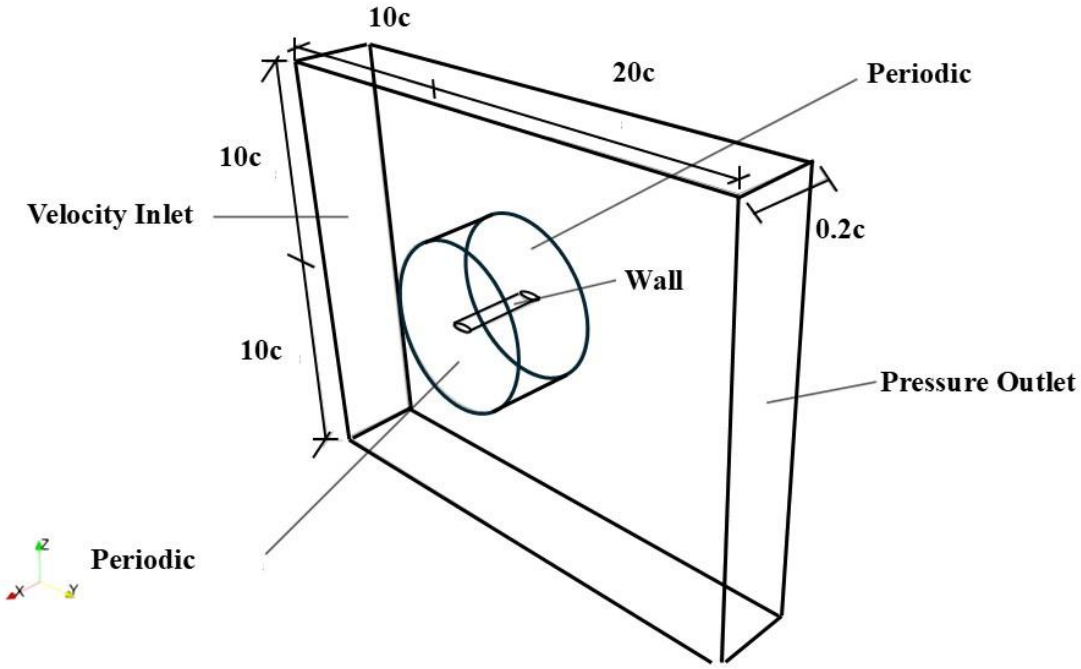

Figure 1 Outline of the Domain Around the Pitching Wing

Some other key studies demonstrated that periodic pitching motion generated the characteristic leading-edge vortex (LEV) and subsequent shedding for dynamic stall to happen. Therefore, this approach enables a more straightforward analysis of the underlying fluid dynamics, making it easier to isolate the influence the birth and growth of vortex structures around the wings on aerodynamics lift and drag forces during the pitching motion. In this study, the leading-edge protuberance is formulated as a sinusoidal spanwise modulation with amplitude A = 0.1c and wavelength λ = 0.2c as (Zhao M. a., 2023):

$$\Delta y(z) = A \sin\left(\frac{2\pi z}{\lambda}\right)$$

This expression is consistent with prior bio-inspired and industrial investigations of tubercled wings. The kinematics of the wings is mathematically described as:

$$\alpha = \alpha_o sin(2\pi f t)$$

here α◦ represents the maximum one-sided amplitude of the oscillation, and its value in our study is 20◦. Besides, f shows the oscillation frequency, and the reduced frequency, defined as

$$k = 2\pi f \frac{c}{V_\infty},$$

is 0.1. Here, V_∞ is the free-stream velocity, and its value is set as $9\ m/s$ at the inlet with c set as 0.083m. We set the span of the wing as 0.2c where the boundary applied to both front and back periodic or cyclic in OpenFOAM (with an infinite aspect ratio):

$$\phi_B = \phi_F, ; \partial_n \phi_F = \partial_n \phi_B$$

To simulate an experimental set-up in a virtual wind tunnel shown in Figure 1. Previous studies have shown that a spanwise periodic domain (shown in Figure 1) of approximately 0.2c is frequently used to emulate an infinite span. It is sufficient to capture the formation, convection, and shedding of coherent stall vortices (as demonstrated in many 2D or quasi-2D studies) and also mentioned previously in by Turner et al. (Turner, 2020) that 0.2c spans do produce the main vortex shedding. Using 0.2c spanwise yields to a better alignment with the objective of capturing the main stall vorticity with minimal effect on spanwise instabilities (Verma, 2023), despite that some literature also cautions that, smaller span, such as 0.2c, will enforce near-2D coherence, potentially overestimating vortex strength and coherence (Sudharsan, 2024), balancing given computation cost of DES. Moreover, the distance of each boundary from the oscillating wing is kept large enough (± 10c in z-direction and − 10c and 20c in the y-direction) to avoid experiencing flow disturbances and numerical instabilities introduced by their

respective neighborhoods (Robertson, 2015), where the inlet boundary condition for inlet is a Dirichlet boundary condition:

$$u = U_\infty; \frac{\partial P}{\partial n} = 0$$

And for outlet is:

$$P = P_{outlet}; \frac{\partial u}{\partial n} = 0$$

Finally, the boundary conditions of top and bottom are symmetry:

$$u \cdot n = 0; \ \frac{\partial u_{\{t_i\}}}{\partial n} = 0$$

To imply that both planes have no normal flow and no shear across the plane.

We perform our numerical simulations around a NACA-0018 wing at $Re = 160,000$, where we define Reynolds number as:

$$Re = \frac{\sqrt{V_\infty^2 + (R\omega)^2} \cdot c}{\upsilon_{air}},$$

where v is the kinematic viscosity of the fluid, and R = 0.5m is set to align with the reference study (Zhao M. a., 2017). At $Re = 160,000$, the flow undergoes transitional behavior that produces the shear-layer instabilities, vortex roll-up, merging, and shedding characteristic of dynamic stall9 in which at high Reynolds number, inertia dominates over viscosity, so small disturbances in the separated shear layer amplify via Kelvin–Helmholtz (K–H) instability (Drazin, 1970). Moreover, dynamic stall experiments and simulations often use Re in the range of $10^5 - 10^6$ for this reason. For instance, experiments on an oscillating airfoil (in a wind tunnel) visualized the classic dynamic stall sequence – from shear-layer roll-up to the formation and shedding of a leading-edge vortex – implying a sufficiently high Reynolds number was used to

trigger these events (Honarmand, 2019). Because our objective is to understand the flow transitions around the wing while it undergoes dynamic stall3, the maximum amplitude is varied from -20° to 20°.

Governing Equations, Turbulence Modelling

We solve the following incompressible forms of the continuity and Navier-Stokes equations using OpenFOAM, which is an open-source finite-volume method based computational solver.

$$\nabla \cdot u = 0$$

$$\frac{\partial u}{\partial t} + \nabla \cdot (u \otimes u) = -\frac{1}{\rho} \nabla p + \nabla \cdot \nu t \, (\nabla u + \nabla u^T) + f$$

Figure 1 shows that we specify a Dirichlet (uniform value) condition for velocity at the inlet and zero-gradient (Neumann) for the pressure. The outlet boundary employs a pressure outlet condition to simulate the outflow, whereas the top and bottom boundaries are defined with a slip boundary condition. Over the wing's surface, the velocity is subjective to no-slip boundary condition while computing pressure using a zero-gradient condition. The boundary condition applied at the front and back planes (spanwise direction) are set to be cyclic (periodic) given that this simulation involves an infinite aspect ratio (Geng, 2018).

Spallart-Allarms Detached Eddy Simulation (DES) and its variants (DDES, IDDES) are well-suited for unsteady flows around airfoils at $Re \sim 160,000$, where flow separation and vortices are formed and shed for the stall phenomenon (Spalart, 2009; Madsen, 2009) and prediction using the equation:

$$\frac{\partial \tilde{v}}{\partial t} + u_j \frac{\partial \tilde{v}}{\partial x_j} = C_{b1}\,(1 - f_{t2})\tilde{S}\tilde{v} + \frac{1}{\sigma}\,\nabla \cdot [(\nu + \tilde{v})\nabla\tilde{v}] + \frac{C_{b2}}{\sigma}\,|\nabla\tilde{v}|^2 - C_{\omega 1}\,f_\omega - \frac{C_{b1}}{\kappa^2} f_{t2} \left(\frac{\tilde{v}}{\tilde{d}}\right)^2 + f_{t1}$$

Where:

$$\tilde{d} = \min(d, C_{DES}\Delta)$$

$$v_t = \tilde{v} f_{v1}$$

$$f_{v1} = \frac{\chi^3}{\chi^3 + C_{v1}^3}$$

$$\chi = \frac{\tilde{v}}{\nu}$$

$$f_{v2} = 1 - \frac{\chi}{1 + \chi f_{v1}}$$

$$f_\omega = \left(\frac{1 + C_{\omega 3}^6}{g^6 + C_{\omega 3}^6}\right)^{\frac{1}{6}}$$

$$g = r + C_{\omega 2}(r^6 - r)$$

$$r = \frac{\tilde{v}}{\tilde{S}\kappa^2 d^2}$$

$$\tilde{S} = S + \frac{\tilde{v}}{\kappa^2 d^2}\, f_{v2}$$

And: $C_{DES} = 0.65$, $C_{\omega 1} = \frac{C_{b1}}{\kappa^2} + \frac{(1 + C_{b2})}{\sigma}$, $C_{\omega 2} = 0.3$, $C_{\omega 3} = 2.0$ and $C_{b1} = 0.135$, $C_{b2} = 0.622$, $C_{v1} = 7.1$, $\sigma = 2/3$ and $\kappa = 0.41$. At this Reynolds number, the boundary layer may transition and separate, which single-equation RANS models struggle to predict, whereas DES can resolve large unsteady eddies in separated regions. Guo et.al (Guo, 2022) compared RANS vs. DES for a

NACA 0018 airfoil (Re 160k) at high incidences. Their DES (SST-DES) captured the unsteady stall vortices and yielded much more accurate forces than steady or unsteady RANS. Similarly, Sun et al. (Sun, 2022) achieved good agreement with experimental results for onset of stall and loading curves predicted deep stall on a thick airfoil (Re $\sim$ 200k). To ensure the precision and consistency requirement of DES, we discretize the flow domain using a structured grid for better control on the sizing of the mesh in different regions, and computational effectiveness (Sun, 2022) and accuracy (Kozelkov, 2016). Using ANSYS ICEM-CFD, the grid is refined through an iterative process carefully, while focusing on areas susceptible to higher levels of flow activity and gradients, as exhibited in Figure 2. Our strategy ensures that even the flow features are full resolved in our simulations. To ensure convergence, numerical accuracy, and the resolution of flow structures in the spanwise direction, guided by previous studies (Spalart, 2009; Tamaki, 2023; MeloMelo De Sousa, 2013), we employ 64 equally-spaced grid nodes over the entire span of the wing (Madsen, 2009). More specifically, the first cell height at the boundary layer treatment near the wall is estimated based on the theory of Kolmogorov's Length Scale (Kolmogorov, 1941; Hunt, 1991) and Schlichting's skin friction formula (Schlichting, 2000) to have a non-dimensional wall-distance y+ less than or equal to 1, which is defined as:

$$\boldsymbol{y}^{+} \cong \left(\frac{v^3}{C_{\mu}^{3/4} \frac{(\frac{3}{2}(U_{\infty} I)^2)^{3/2}}{0.07\mathrm{c}}} \right)^{1/4}$$

Where $v = 1.5 \times 10^{-5} \frac{m^2}{s}$ is the kinematic viscosity of air, $C_{\mu} = 0.09$ representing the RAS turbulent model constat, and $I = 0.01$ being the turbulent intensity of 1%.

Furthermore, the mesh is generated with an extreme level of care, where it undergoes a slow and smooth transition from the wing's surface to the trailing edge arc, as presented in Figure 2 and Figure 3. This control over mesh generation is particularly crucial in the transition or "grey" region, which often poses challenges, such as Modelled Stress Depletion (MSD) (Travin A. a., 2000) and Grid-Induced Separation (GIS), addressed by Menter and Kuntz (Menter, 2004)In these mesh regions, where computations for LES are performed, having isentropic grid is of great importance to avoid the afore-mentioned problems.

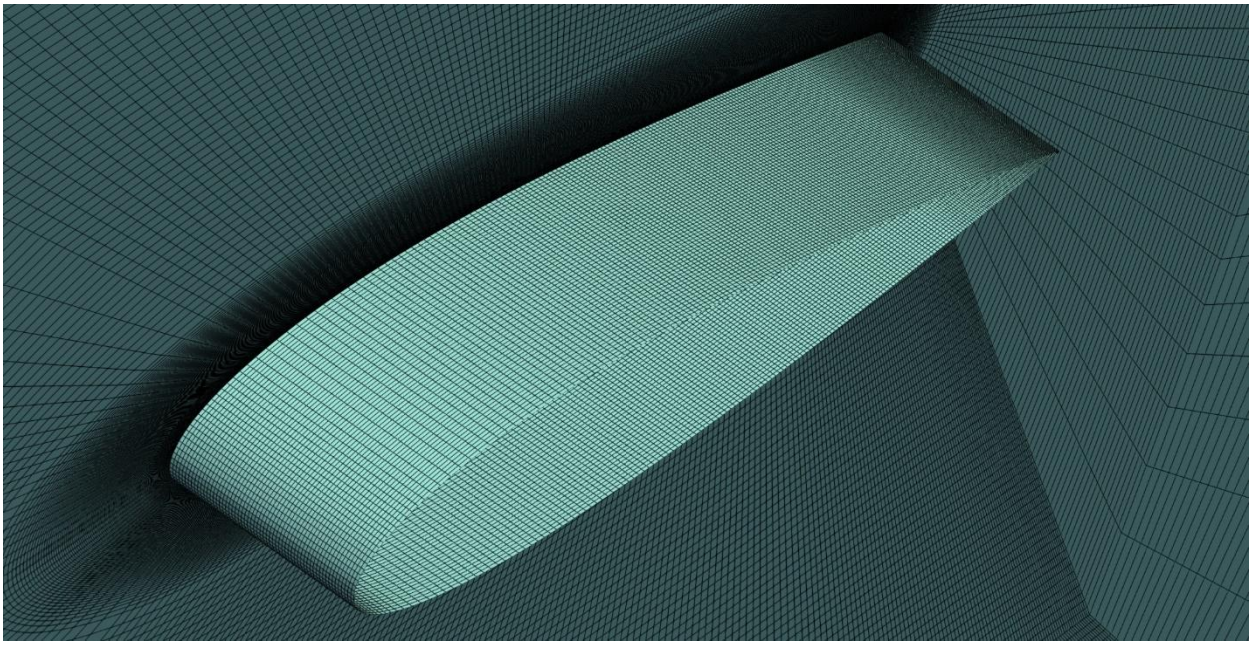

Figure 2 An isometric view of the mesh closer to the surface of the NACA 0018 wing

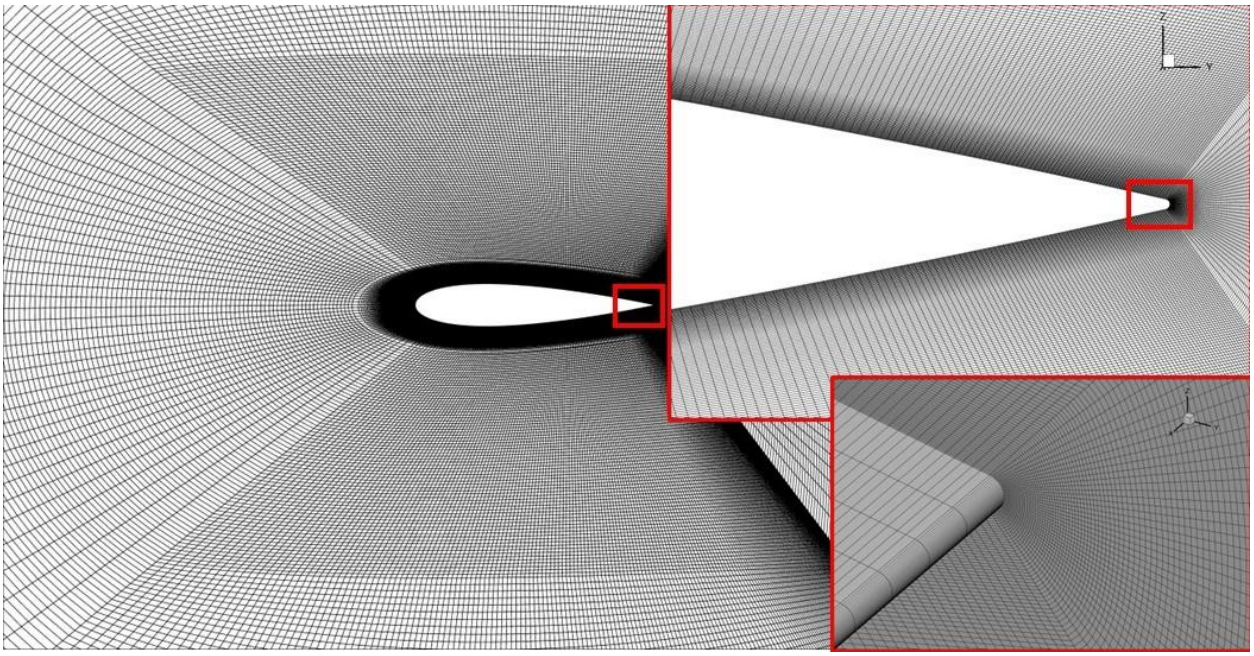

Figure 3 zoomed-in view of the mesh on the trailing-edge of the wing

Numerical Schemes:

This section details the full finite-volume discretization formulations for the four key schemes shown—time derivative (Euler), gradient (cell-Limited Gauss linear 1), divergence (Gauss linear), and Laplacian (Gauss linear corrected)—as implemented in OpenFOAM's fvSchemes dictionary. We give the integral or pointwise expressions, define all interpolation and limiter parameters, and cite official OpenFOAM documentation for each component.

Specifically, the transient and temporal terms are discretized implicitly over a time step Δt using a backward-Euler approximation:

$$\left.\frac{\partial \phi}{\partial t}\right|_P \approx \frac{\phi_P^{n+1} - \phi_P^n}{\Delta t}$$

The face-centered approximation of the gradient at an arbitrary cell P is:

$$\nabla\phi|_P = \frac{1}{V_P}\sum_{f\in P}\phi_f S_f,$$

where V_P is the cell volume and S_f the outward face area vector of the arbitrary cell P and with an underlying interpolation:

$$\phi_f = \frac{1}{2}(\phi_P + \phi_N)$$

With the limiter ϕ_f^{limited} and β:

$$\phi_f^{\text{limited}} = \phi_P + \beta(\phi_f - \phi_P),$$

$$\beta = \min\left(1, \frac{|\phi_N - \phi_P|}{|\phi_f - \phi_P|}\right)$$

Which prevented overshoots by blending with the cell-value ϕ_f^{limited} and A factor of 1 guarantees boundedness, clipping face values to lie within: $\max(\phi_N, \phi_P)$ and $\min(\phi_N, \phi_P)$.

The divergence of a flux field F over a control volume V is approximated via Gauss's theorem:

$$\int_V \nabla \cdot F dV = \sum_f F_f \cdot S_f$$

with central interpolation function:

$$F_f = \frac{1}{2}(F_P + F_N)$$

Additionally, the diffusive term is discretized as:

$$\nabla \cdot (\Gamma \nabla\phi) = \sum_f \Gamma_f (\nabla\phi)_f \cdot S_f$$

where face diffusivity is interpolated linearly as:

$$\Gamma_f = 0.5(\Gamma_P + \Gamma_N).$$

The face-gradient $(\nabla\phi)_f$ uses the "corrected" non-orthogonal approach:

$$(\nabla\phi)_f = (\nabla\phi)_f^{orth} + \left(I - n_f n_f\right) \cdot \nabla$$

with the orthogonal component:

$$(\nabla\phi)_f^{orth} = \frac{\phi N - \phi P}{|\, d \,|}\boldsymbol{n}_f$$

Validation and Verification

Since the primary focus of our current work is to investigate changes in vortex dynamics during pitching motion, it is essential that the mesh accurately captures the complex flow phenomena, including vortex shedding, boundary layer separation, and reattachment, while minimizing the associated computational costs. To attain grid-independent solutions, three mesh configurations are tested, each with progressively finer resolutions. The process begins with a coarse grid, having 6 million cells, to establish a baseline, followed by medium and fine meshes with increasing numbers of grid cells concentrated around the airfoil surface and in the wake region where vortex structures are formed. The medium and fine meshes are composed of 8 million and 10 million cells, respectively. Special attention is given to refining the mesh in near-wall regions, ensuring that the boundary layer is well-resolved by using appropriate wall functions or y^+ values, typically below 1 (Tamaki, 2023), as mentioned above.

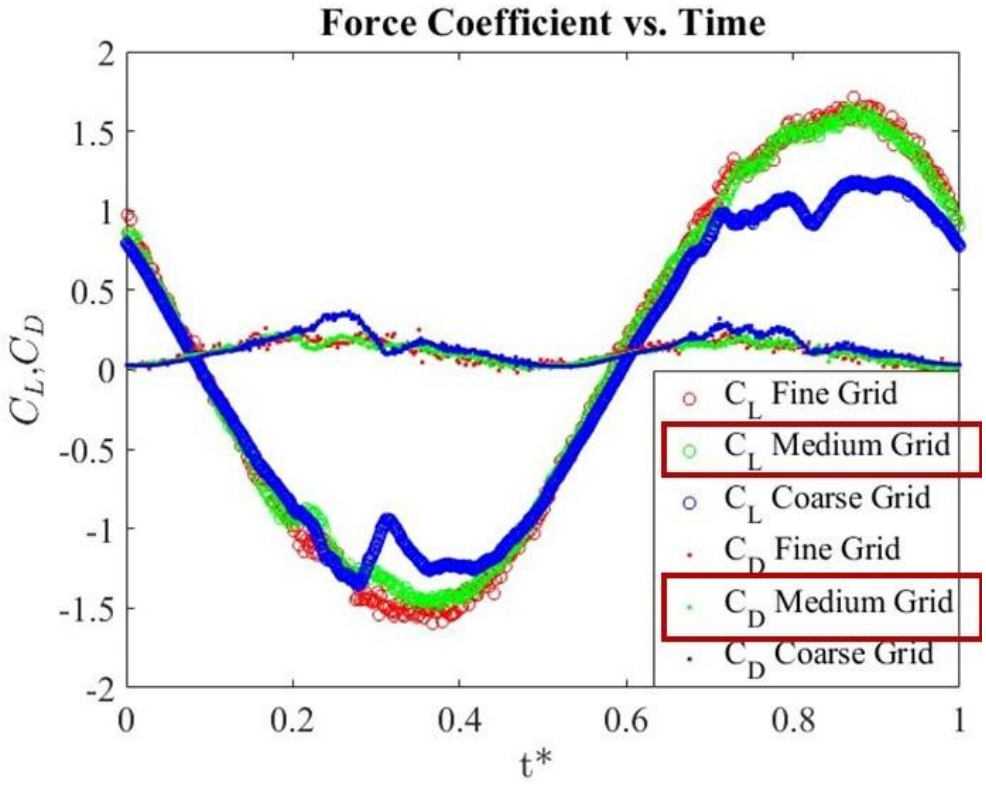

Figure 4 results for the grid-independence study of the last oscillation cycle

Here, the lift coefficient C_L and drag coefficient (C_D) is the primary metrics used to assess convergence of the grid, which is a common approach to verify the validity of the current study, given the confidentiality of the data, such as velocity profile as shown in Figure 4. The global nature, as compared to velocity profiles, of C_L and C_D makes them particularly sensitive to overall flow features such as separation bubbles, laminar–turbulent transition, and large-scale vortical structures, which are precisely the phenomena verification and validation aims to capture in our work. As presented in Figure 4 and Figure 5, it is evident from the profiles of C_L and C_D that the computational results a significant change when the mesh size is increased, while moving from the coarse to the medium grid. Beyond the medium mesh, the results do not experience a significant change. This final mesh provides a good balance between computational efficiency and accuracy. It ensures that that the results, particularly the behavior

of the leading-edge vortices (LEVs) and trailing-edge vortices (TEVs), are not dependent on the grid structure but are instead reflective of the true physical phenomena of interest. To ensure the accuracy and stability of our simulations, a time step-convergence study is conducted by varying the number of time steps per oscillation cycle as shown:

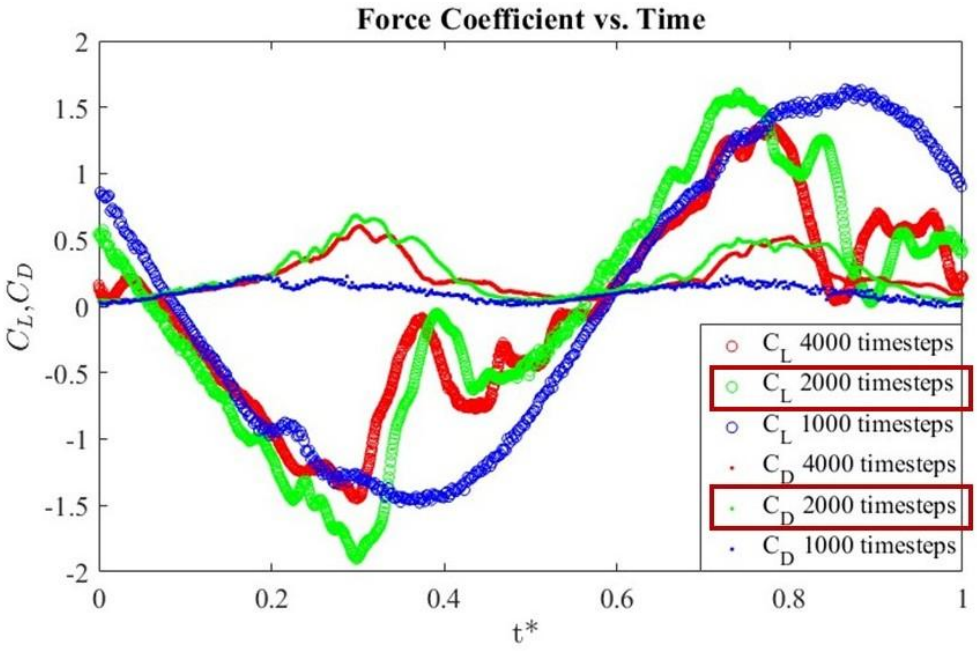

Figure 5 results for the timestep-independence study of the last oscillation cycle

these simulations are performed with 1,000, 2,000, and 4,000 time-steps per oscillation cycle to evaluate the impact of temporal resolution on the results. The analysis revealed that the case with 1,000 time-steps exhibits noticeable discrepancies, particularly in capturing the dynamic stall characteristics and vortex shedding timing, due to insufficient temporal resolution. The case with 2,000 time-steps demonstrates a significant improvement, sufficiently matching (Geng, 2018). The results from the case with 4,000 time-steps with minor discrepancies in transient flow features, such as the reattachment phase after stall. The differences may be due to the hysteresis effect (Williams, 2017) and nonlinear nature of the

turbulent flow around the pitching airfoil at the currently considered very high Reynolds number. Nevertheless, the improvements are marginal compared to the computational cost incurred.

Validation studies using a NACA 0012 wing remains a cornerstone in advancing our understanding of unsteady aerodynamics, providing critical benchmarks for computational methods. According to Jacobs et al. (Jacobs, 1933), while the thickness-to-chord ratio does affect the maximum lift and drag coefficients, the general aerodynamic trends remain comparable, especially at moderate angles of attack. Moreover, according to Abbott et al. (Abbott, 2012), symmetrical airfoils within the same series exhibit similar characteristics in boundary layer transition and flow separation in low-speed, incompressible flows, despite differences in thickness of wings. While acknowledging that variations in thickness can impact certain aerodynamic parameters, the evidence suggests that a NACA 0012 wing can provide valuable insights into the performance of a NACA 0018 wing. Lee and Gerontakos (Lee, 2004) conducted extensive experimental investigations, capturing detailed aerodynamic forces and flow structures during pitching and plunging motions of wings. Their work serves as a reliable reference for validating computational methodology. Additionally, Wang et al. (Wang S. a., 2012) employed DES to model the similar cases, demonstrating the capability of hybrid turbulence models to predict unsteady vortex dynamics and wake structures. However, the grid resolution in their study remained limited, particularly in terms of time step size and grid refinements. They performed their simulations using 800 time-steps per oscillation cycle (Wang S. a., 2012). These limitations possibly caused discrepancies between their simulation results and the experimental data, especially in capturing high-frequency dynamics of small turbulent

flow structures and the rapid flow transitions during dynamic stall (Honarmand, 2019), as shown in Figure 7. Our currently obtained results exhibit significant improvements in comparison to the study of Wang et al. by employing finer resolutions in time-steps and more refined grids. This enhancement allows the simulation to run smoother, reducing numerical diffusion and better resolving transient flow features. Consequently, the current DES results show much closer alignment with the experimental data from Lee et al (Lee, 2004) particularly in predicting peak aerodynamic forces presented in Figure 6 and capturing the temporal evolution of coherent flow structures.

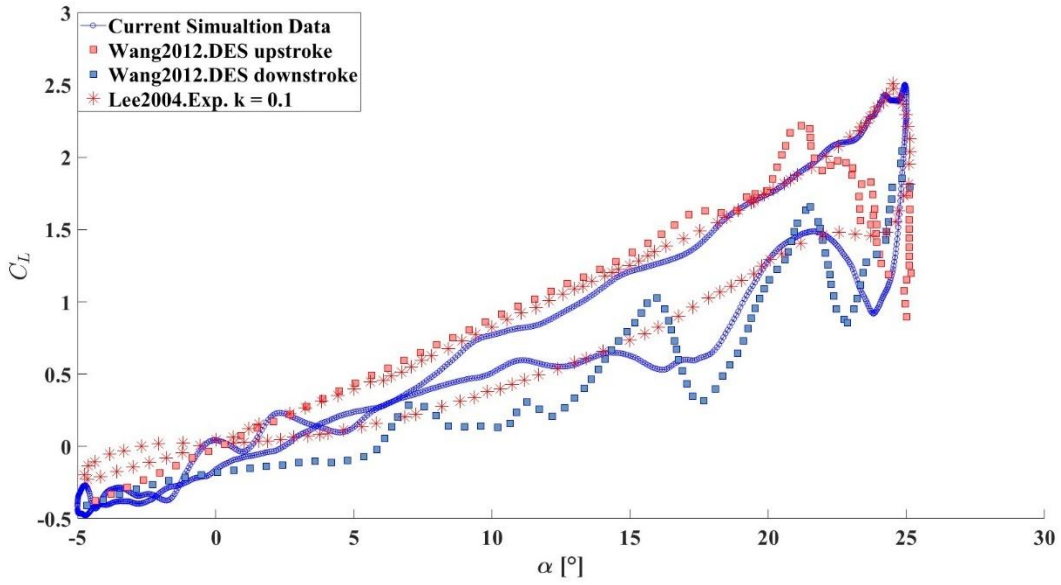

Figure 6 Validations of profiles of C_L from our present simulation methodology with previous studies

Chapter 3

Proper Orthogonal Decomposition

Chapter 3 introduces the application of Proper Orthogonal Decomposition (POD) to three-dimensional velocity data extracted from the standard pitching-airfoil simulations. By decomposing the unsteady flow into orthogonal modes ranked by kinetic energy, POD isolates dominant coherent structures—such as leading-edge separation bubbles, shear-layer vortices, and wake instabilities—that govern dynamic stall behavior. In our study of proper orthogonal decomposition (POD), we carefully extract the data in the rectangular pitching zone in which the airfoil geometry is located as shown in Figure 1 previously. The three velocity components (u, v, w) at each grid point are assembled into a large data matrix, which is then subjected to singular value decomposition (SVD) to yield spatial modes and accompanying temporal coefficients. The resulting singular values quantify each mode's energy content, facilitating selection of a reduced set of modes that capture the bulk of turbulent kinetic energy.

Mathematical Model:

In our study of proper orthogonal decomposition (POD), we carefully extract the data in the cylindrical pitching zone in which the airfoil geometry is located as shown in Figure 1. previously. The domain spans $\pm 0.25\ c$ in the longitude (z) direction and from $-0.25\ c$ to $1.5\ c$ in the chordwise (x) direction, discretized on a uniform $60 \times 150 \times 150$ grid after rotating each snapshot to align with the instantaneous pitch angle. Due to the data-driven nature of the technique, we carefully extract the data according to its angular position at their corresponding time-step snapshots by rotating the larger domain and then performing linear interpolation to the inner domain. Even though it is voluntary to make the time-average profile exclusive (Khalid, 2020), the implementation is carried out for better accuracy and flow field kinematics

around the wing through a decomposition into a $(N_U + N_V + N_W) \times N_T$ matrix. Once the velocity field is adequately aligned, we construct a velocity matrix, where each row corresponds to a spatial location, and each column represents a snapshot in time. The velocity matrix is then subjected to singular value decomposition (SVD) to extract the dominant modes:

$$X_s = U\Sigma V^T$$

Where U, and V are the unitary matrices, containing the left eigenvectors and temporal variations of X_S, in which the column vectors give us the spatial distribution in each of the modes and temporal coefficient from U and V respectively (Wang Z. a., 2012). The resulting diagonal singular values matrix represents the energy content of each mode, which are subsequently ranked in descending order:

$$\sigma_1 \geq \sigma_2 \geq \sigma_3 \ldots \geq \sigma_N$$

to identify the most energetic and dynamically significant flow structures to distinguish between dominant and secondary modes, and analyze the role of turbulence in energy dissipation across different regions of the wake.

Results and Discussion:

Vortex Dynamics:

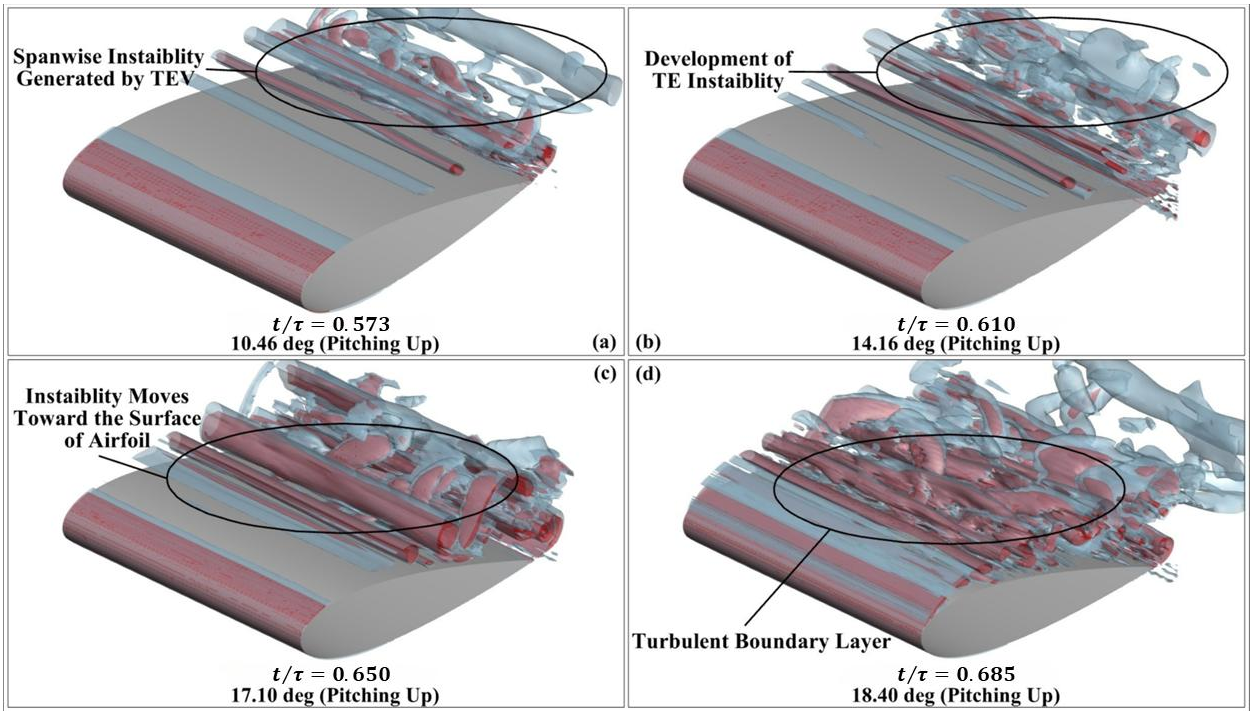

Figure 7 -dimensional iso-surfaces of Q values at (a) t/τ = 0.573, (b) t/τ = 0.610, (c) t/τ = 0.650, and (d) t/τ = 0.685 where the red- and blue-colored flow structures represent Q = 5000 and 2000, respectively

The behavior of vortex structures around a pitching airfoil is a critical determinant of its aerodynamic performance and the dynamic stall conditions. Figure 7 shows the formation, transition, and dynamics of coherent flow structures at different stages of the pitching motion of the wing. At the very beginning of the pitching cycle, the trailing edge vortices remain relatively stable, with minor span-wise disturbances localized near the wake region (see Figure 7a). We observe a spanwise instability in the TEV at 10.46◦ in Figure 7b when the wing continues pitching up. The instability further grows and travels upstream while the wing still undergoes its upstroke for α ≤ 18.4◦. Beyond a critical threshold, lying between 17.5◦ − 18◦ angle-of-attack, this instability triggers a cascading effect similar to a “domino effect”, where the initially

coherent vortex system collapses into irregular turbulent structures, as depicted in Figure 7d. This process is particularly significant in the dynamic stall phenomenon, as the loss of coherence in vortices amplifies fluctuations in unsteady loads and aerodynamic hysteresis, which are challenging to predict using conventional modeling approaches.

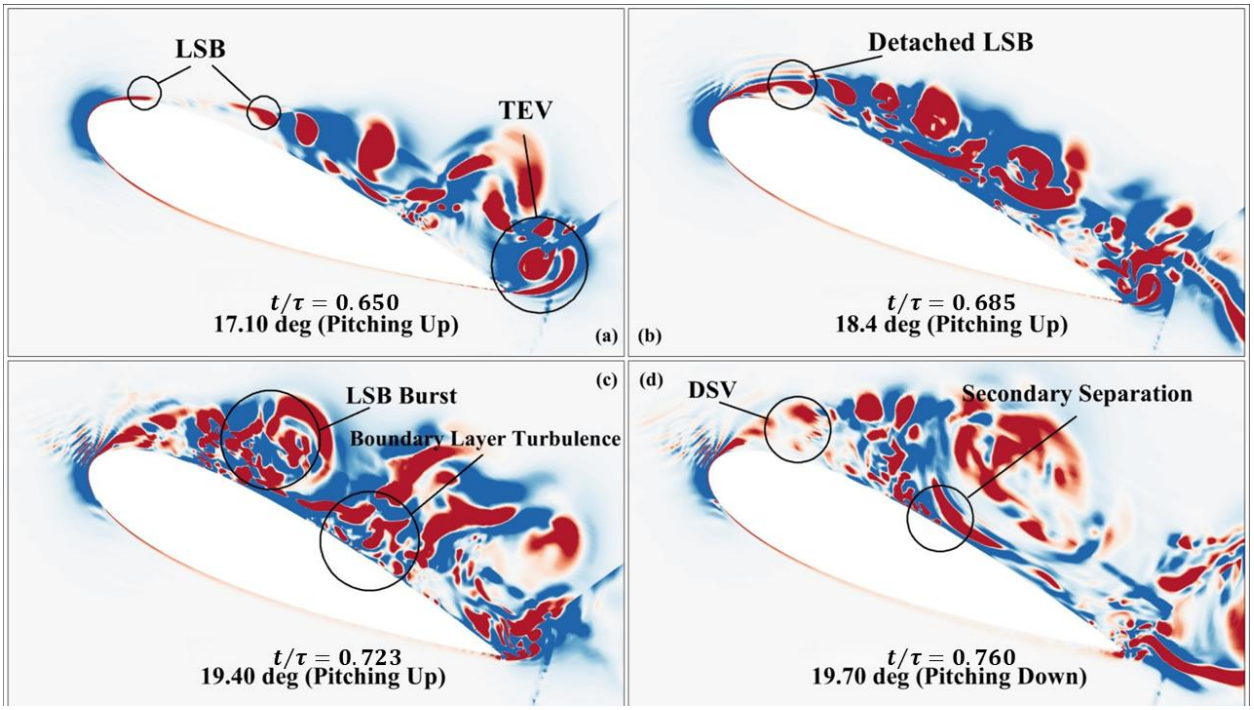

Figure 8 Two-dimensional contours of positive (in red) and negative (in blue) Q values on the mid plane of the flow domain at (a) t/τ = 0.650, (b) t/τ = 0.685, (c) t/τ = 0.723, and (d) t/τ = 0.760

At a high Re of 160, 000, the presence and evolution of a leading-edge separation bubble (LSB) play a vital role in controlling the pressure distribution over the airfoil surface (Visbal, 2018) The growth of the instability from the trailing part of the wing strongly influences the flow behavior at its leading part (Menon, 2021) We explain different stages in this process using contour plots of the pressure coefficient (see Figure 9) and Q-values (see Figure 8) around the wing in the mid-plane of the flow field. During the initial phase of the pitching motion, the LSB remains attached to the leading edge, maintaining a high-pressure difference between the upper and lower surfaces due to the sustained boundary layer attachment. However, as the

pitching angle increases beyond approximately 18.4◦ − 18.9◦, the pre-burst of LSB occurs, as shown in Fig. 7c through a large low-pressure zone and in Figure 9c through the positive and negative values of the Q-value at the solution time of t/τ = 0.685 It is important to point out that positive and negative Q values highlight the flow regions with stronger rotation and shear strain, respectively. At the stall angle of 19◦ in (t/τ = 0.74), the LSB undergoes a sudden burst, triggering dynamic stall. This phenomenon occurs because, beyond a critical angle-of-attack (19◦ in this case), the vortical structures lose coherence, failing to follow a stable convective trajectory along the wing's surface. Consequently, flow around the wing becomes highly chaotic, leading to unstructured turbulence all along the surface and causing abrupt aerodynamic force fluctuations and lift breakdown.

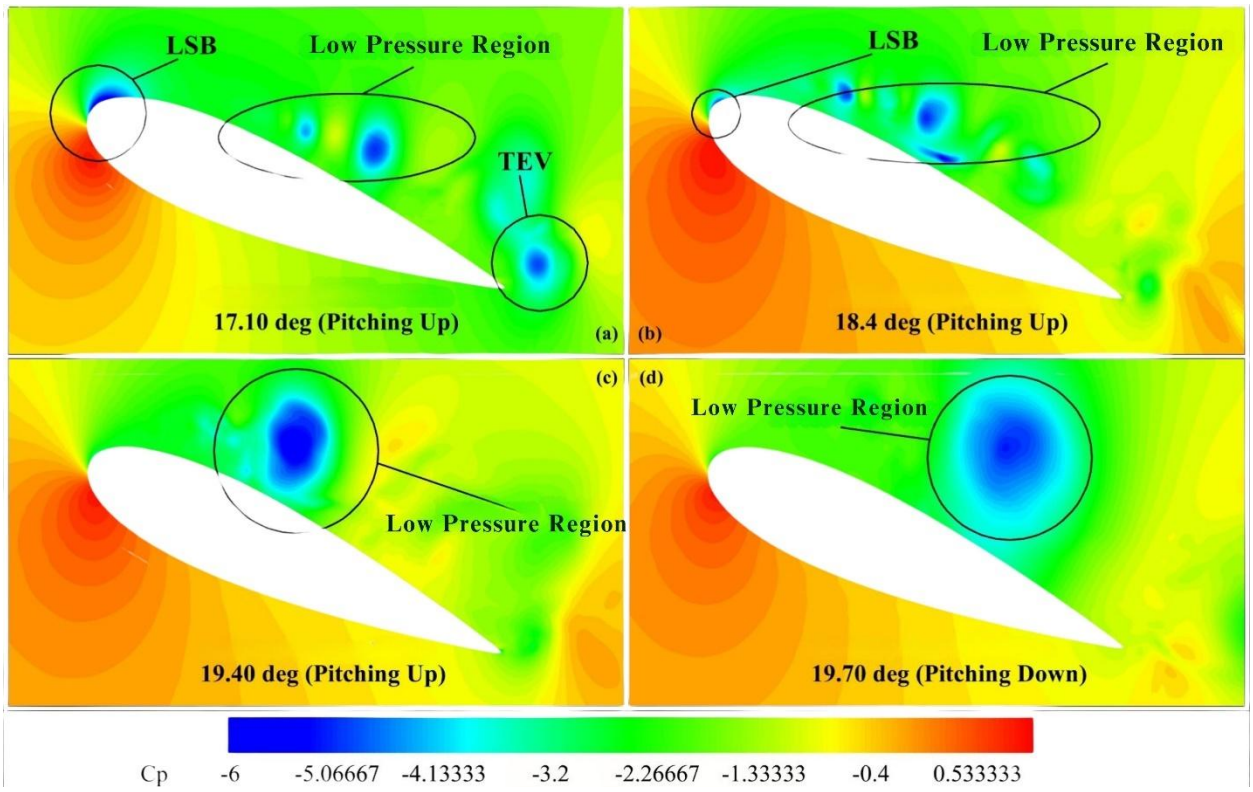

Figure 9 Pressure coefficient contour at (a) t/τ = 0.650, (b) t/τ = 0.685, (c) t/τ = 0.723, and (d) t/τ = 0.760.

Before onset of stall, the pressure distributions around the wing in Figure 9a and b remain relatively regular. More specially, distinct leading-edge suction peaks are observed at these time instants, indicating that the boundary layer is still largely attached to the surface with a LSB present near the leading edge (Visbal, 2018). This bubble maintains favorable pressure gradients, supporting lift generation. Additionally, small-scale surface pressure voids and trailing-edge vortices (TEVs) can be identified in the middle zone of the wing along the chord. These structures maintain a constructive difference in pressure between the upper and lower surfaces, ensuring a stable lift force.

As the airfoil continues pitching up (see Figure 9 at $t/\tau = 0.723$), the flow structure undergoes a rapid transition process. The low-pressure region (shown in Figure 9a - d), which previously remain distinct and separated, merge into a single large low-pressure region above the surface of the wing. It occurs as the LEV grows and coalesces with smaller vortical structures, effectively causing low pressure in the surrounding to make the local air flow into this region. Additionally, the collapse of the large pressure difference between the upper and lower surfaces of the wing results in a sudden fluctuation in the aerodynamic load, which can induce undesirable structural vibrations. In Figure 9d, the airfoil begins pitching downward, and the merged low-pressure zone still remains dominant, and the reattachment of the flow with the wing gets delayed. This results in a sudden drop in the lift force, which is a signature of dynamic stall. The strong adverse pressure gradient at the leading edge causes complete flow separation, and no

coherent high-suction region is maintained on the top surface of the wing.

Further insights are gained from the two-dimensional mid-plane contour analysis of vortex and shear flow structures presented in Figure 8, where Q-criterion is employed to distinguish between coherent vortex regions ($Q > 0$) and shear-dominated regions ($Q < 0$). At $t/\tau = 0.650$ (see Figure 8a), vortex structures dominate the flow around the wing, reinforcing the stability of the attached boundary layer. However, as the pitching motion progresses, the LSB starts getting detached from the upper surface. Apparently, it leads to a growing competition between vortex-induced flow and shear-driven separation, as shown in Figure 8b. Initially, the vortices maintain their dominance. With α increasing to the stall angle, the influence of shear instabilities from the trailing edge intensifies, where only the minor vortex structures lose their coherence. With the instabilities further propagating upstream shown in Figure 8c and d, they "erode" the structured vortex regions, where the vortex structure of the main LSBs start to turn into smaller turbulent eddies. This progressive shift in the dominant flow regime is caused by the low-pressure zone left by the bursting of LSB from the leading edge. Ultimately, the instabilities prevail at high α, and a dominant shear flow activity is noticed over the upper surface of the airfoil, highlighting the full onset of dynamic stall.

Proper Orthogonal Decomposition:

The interplay between vortex evolution and shear instability highlights the inherent complexity of unsteady aerodynamics of pitching airfoils. The transition from a vortex-dominated flow to a shear-dominated regime is highly nonlinear, dictated by the competition between leading-edge separation dynamics and the amplification of trailing-edge instabilities. This shift has significant implications on aerodynamic performance, as it directly influences lift, drag, and pitching moment hysteresis (Menon, 2021). Understanding these mechanisms not

only aids in refining CFD models but also provides critical insights for the development of flow control strategies aimed at mitigating the adverse effects of dynamic stall. Employing advanced modal decomposition techniques, such as proper orthogonal decomposition (POD), further enhances our ability to characterize, categorize, and predict complex flow features governing the aerodynamics of pitching wings. By identifying the dominant modes and their associated flow features, engineers can focus on optimizing specific aspects of the wing's performance. For example, reducing the energy in higher modes associated with turbulence might lead to quieter operation, while controlling the vortex shedding modes could improve efficiency or reduce fluctuations in unsteady forces. Furthermore, the reduced-order models developed using POD can serve as the basis for real-time flow control strategies, such as active feedback systems for mitigating flow separation (Akhtar, 2008).

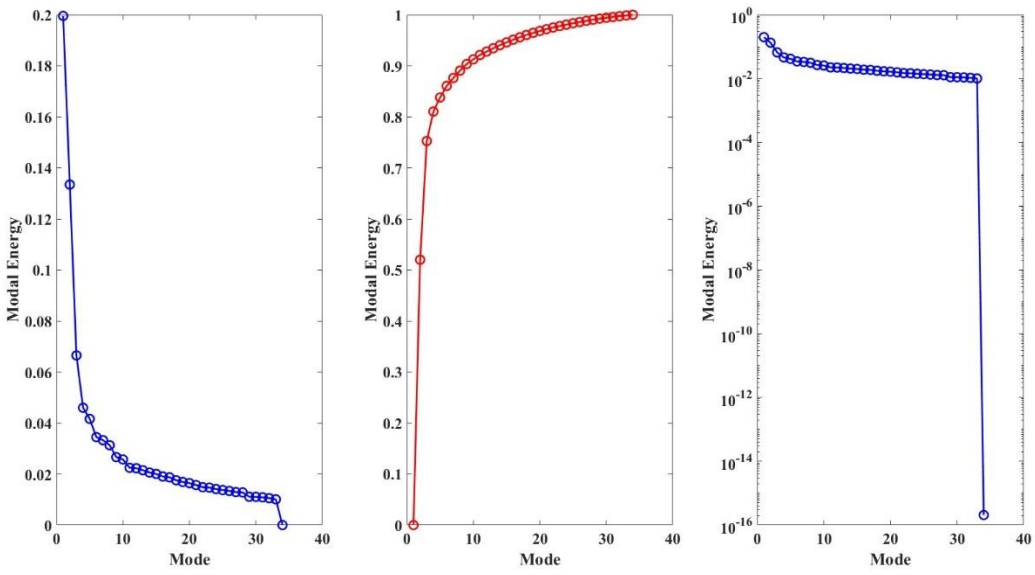

Figure 10 Modal energy(a) cumulative energy (b) modal energy in logarithm scale (c) and as a fraction of the total energy

Figure 10 presents how much influential different POD modes are in terms of their contributions to the total energy of the system. Because of the high-Re-flow, we notice that at

least 15 modes are needed to capture 98% of the total energy. Next 22 modes do not seem to be big contributors in this process. We plot the Q-values extracted from the velocity-based POD modes in Figure 12 and Figure 13. The modal reconstruction is performed for the sake of accuracy and reliability. Figure 11 illustrates how successively bringing more POD modes progressively reconstruct the wake of the blade, first resolving only the strongest leading-edge dynamic-stall vortices and then adding the fainter trailing-edge structures. In Figure 11a, the snapshot reconstructed for $t/\tau = 0.45$ with just Modes 1–3 captures the primary leading-edge vortex, but only hints at the weaker, more diffused trailing-edge vortices seen in the true flow (see Fig. 10d), contributing 50% of the total kinetic energy. By increasing the kinetic energy level to 75%, incorporating Modes 4 and 5 in the flow field (see Figure 11b) brings the largest trailing-edge vortex into view, albeit with under-resolved size and position. Finally, the ninth-mode (90%) reconstruction in Figure 11c nearly reproduces both the compact leading-edge vortex cores and the finer trailing-edge vortex coherence, closely matching the full instantaneous field presented in Fig. 10d. This clear improvement from addition of modes reflects the cumulative kinetic energy captured by the POD expansion refines the wake's spatial detail and alignment with the true flow.

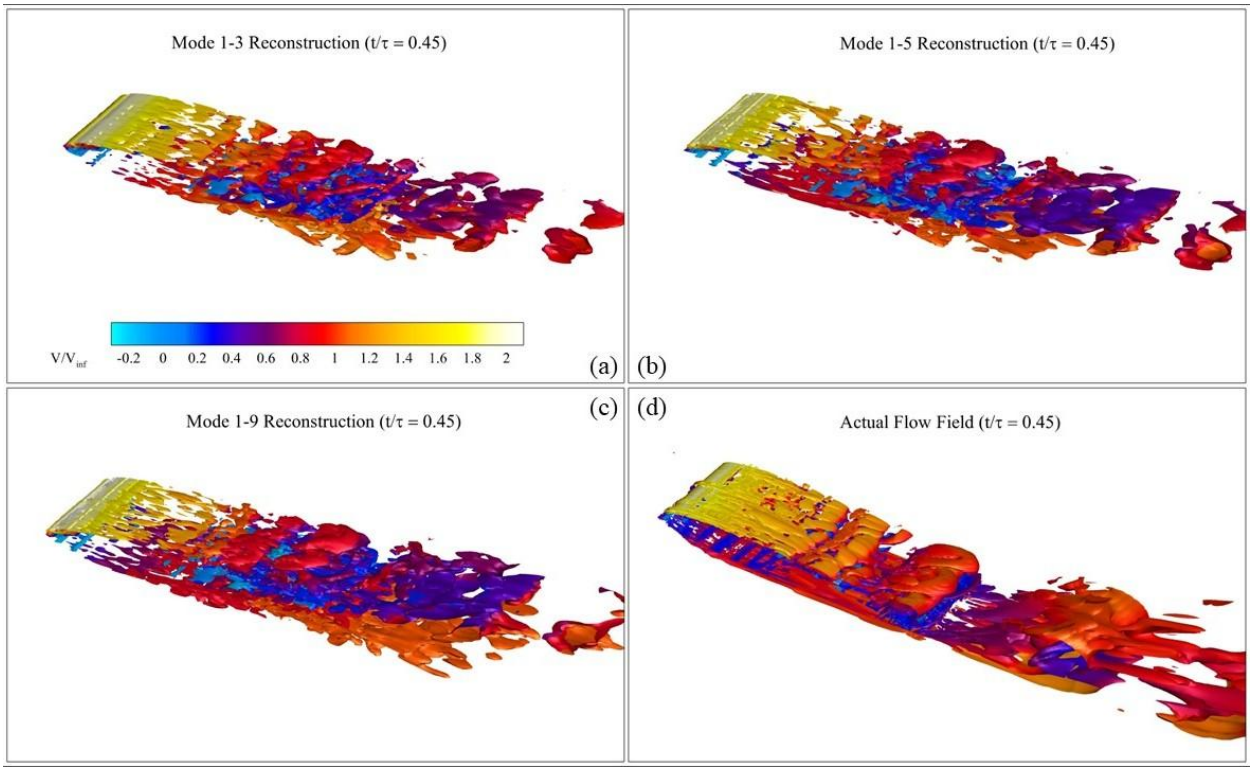

Figure 11 Cumulative Modal Reconstruction from (a) Mode 1-3 (54% Kinetic Energy), (b) Mode 1-5 (75% Kinetic Energy), (c) Mode 1-9 (90% Kinetic Energy), and Comparison with the Original Flow (d) at t/τ = 0.450 plotted using iso-surfaces of Q = 2000 coloured by V/V_∞

POD Mode 1 captures the large-scale vortex formation near the leading edge of the airfoil (see Figure 11a), which is the most energetic mode (20%) of turbulent kinetic energy. Physically, this mode often corresponds to the primary large coherent structure or separation bubble, that forms around the leading edge during the pitching motion under these flow conditions. This separation bubble is a critical aerodynamic feature because it dictates the onset and extent of flow separation and reattachment, directly influencing the dynamic stall process, as discussed earlier. The coherence of this structure visualized through three-dimensional iso-surfaces of Q-criterion (stronger vortices in red with Q = 0.5 and weaker vortices (with Q = 0.1) highlights the importance of Mode 1 in forming the flow energy and governing the dynamics at the leading

edge. This coherent structure facilitates the initial roll-up of the shear layer, forming the foundation for the development of secondary vortices and wake dynamics.

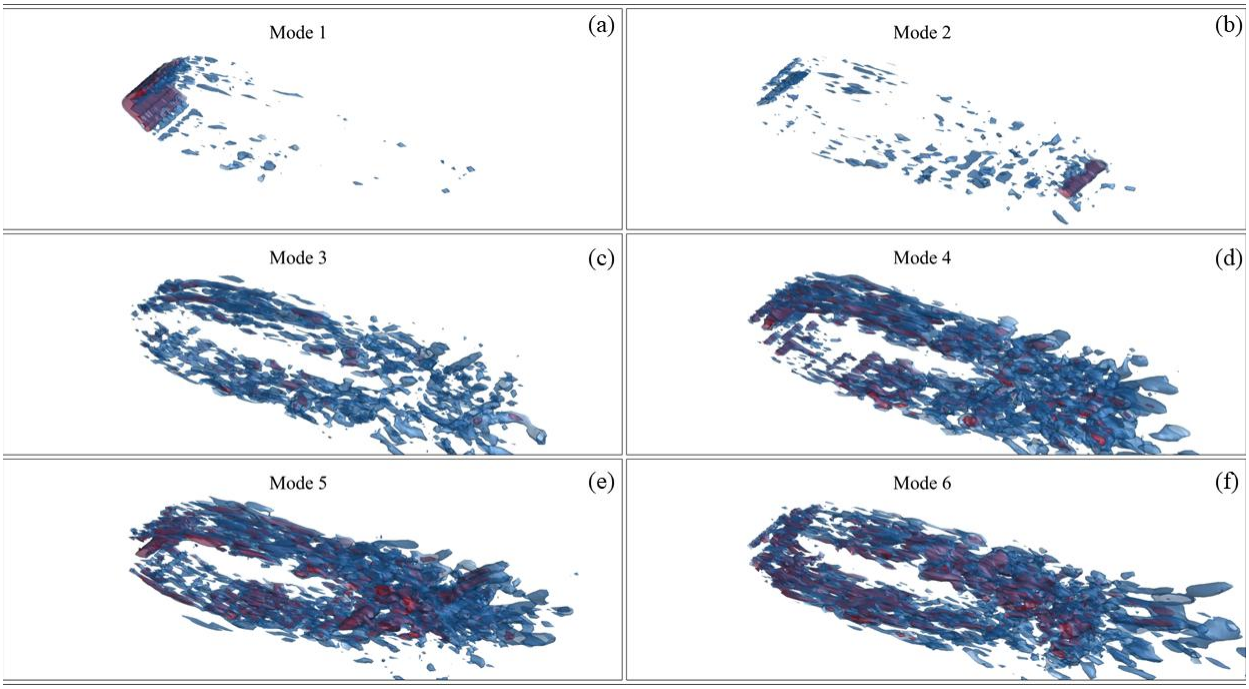

Figure 12 Iso-surfaces of Q-criterion computed through velocity POD modes 1 – 6 where blue and red structures represent the Q values of 0.1 and 0.5, respectively

Furthermore, the most intense flow activity, including vortex formation, LSB, and spanwise flow instabilities, occurs on the leading and trailing edges. These regions dominate the kinetic energy of the flow, which are captured as the most energetic modes in POD.

The second mode exhibits the formation of flow features around the trailing edge in Figure 12b that also involve some secondary structures in the leading and trailing zones. These vortices are less coherent than those captured in Mode 1(see Figure 12a to b). The mode 2 captures the dynamics of vortices that shed from the trailing edge, which usually plays a critical role in wake development and overall flow instabilities. The Q values-based visualizations associated with Mode 2 show smaller and less coherent structures compared to Mode 1,

indicating the downstream propagation and dissipation of these vortices. These TEVs ultimately interact with the wake, contributing to oscillatory forces and the periodic shedding characteristic of unsteady flows. Mode 3 to mode 6 capture shear layer instabilities and finer-scale turbulence, as shown in the plots of the last two rows in Figure 12c - f. These higher-order modes depict localized, transient phenomena that emerge from the interactions of primary vortices with the surrounding flow, e.g. LSB transforming into smaller turbulent bubbles during dynamic stall). The fragmented nature of the vortices in these modes is evident here, which show dispersed and less coherent vortical structures. These shear-layer instabilities, mentioned previously, possibly represent energy cascade to smaller scales, which is a characteristic feature in transition to turbulence. Although their energy contributions are individually less compared to modes 1 and 2, these modes are critical to understanding the onset of turbulence and its influence on the flow dynamics, as they collectively constitute 15% of the turbulent kinetic energy.

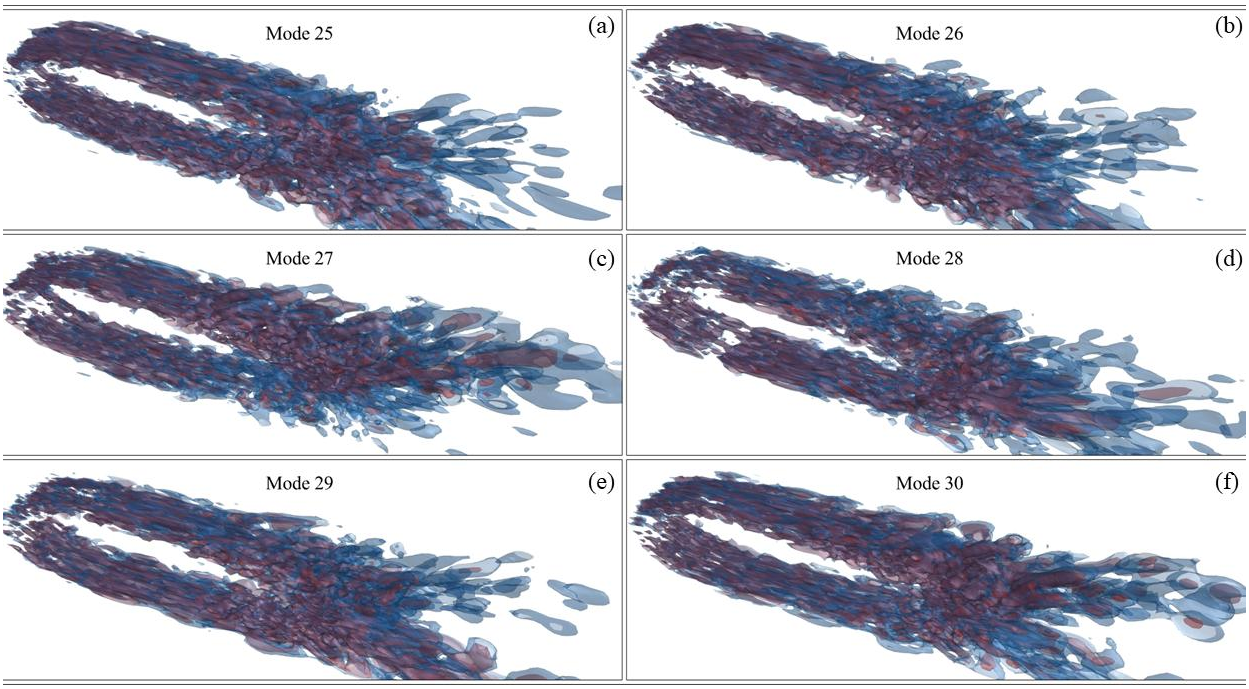

Figure 13 Iso-surfaces of Q-criterion computed through velocity POD modes 25 -30 where blue and red structures represent the Q values of 0.1 and 0.5, respectively

As the order of the POD modes increases beyond 25, the visualizations in Figure 13 begin to show a pronounced shift in the flow activity, gearing it towards the wake region. It is apparent that that higher-order modes primarily capture wake dynamics and turbulent dissipation, rather than coherent vortex structures near the wing's surface. The energy content of these modes is substantially lower, reflecting their role in representing small-scale, chaotic flow features in the wake. This shift implies a transition from dominant aerodynamic features to the finer details of wake turbulence, providing a comprehensive picture of the energy cascade in the wake region. Q-criterion visualizations which are mentioned previously confirmed that, during stall, the flow transitions from coherent vortex structures to large-scale turbulence. The organized shedding of leading-edge vortices in the pre-stall condition breaks down into chaotic, broadband turbulence in the stall phase. It could potentially result as a flow intensifier to

increase the spanwise instabilities and the production smaller eddies, which are further discussed in Figure 12 - Figure 15.

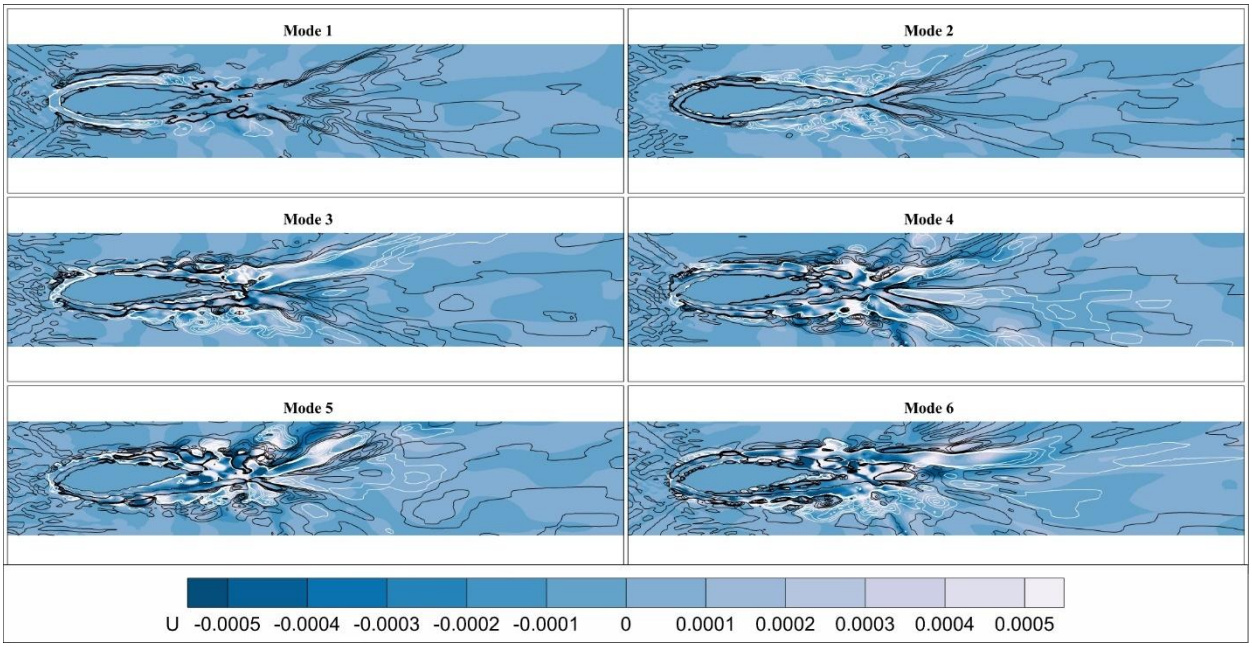

Figure 14 The six most energetic modes. Positive and negative spanwise velocity components are displayed in white and blue respectively, and are overlaid with contours representing streamlines of clockwise and counter clockwise rotation (black and white, respectively)

Velocity and vorticity contours offer complementary perspectives to the POD analysis, enriching our understanding of the flow field dynamics. The two-dimensional velocity fields reveal prominent flow structures, such as the separation and reattachment zones near the leading and trailing edges. High velocity gradients near the leading edge corroborate the dominant energy contribution of Mode 1, aligning with the initiation of vortex shedding. In contrast, the trailing edge regions display more complex velocity distributions, shaped by the wake interactions and oscillatory nature of the airfoil motion. Velocity contours shown in Figure 14, particularly the spanwise-velocity com- ponents (U), provide a more granular view of the span-wise flow dynamics to help visualize the flow instabilities, especially in the spanwise direction introduced by the trailing edge vortices instabilities mentioned before (see Figure 7a -

d). Not only, these flow-instability characteristics are further confirmed by Q-criterion contours on the middle plane in Figure 14. On the other hand, positive and negative vorticity components, along with the q-criterion contour in Figure 14 - Figure 15 gives the perspective to the viewers that when the span-wise instabilities are introduced, the behaviors and coherence of the vortex on the leading edge and on the surface of the airfoil. Specifically, we find from Mode 1 to Mode 2, the positive x-vorticity (highlighted in white in Figure 14) is shifted from the leading edge region to the trailing edge region, which matched with the Q-criterion where we argued that the coherent vortex were mainly "colonized" on the leading edge rather than the trailing edge for Mode 1, and vice versa for Mode 2. It is important to note that spanwise flow instabilities in Modes 1 and 2 are lower shown in Figure 14, as the spanwise flow velocity in relatively low compared to the higher order modes. It can also be confirmed in Figure 15 where pockets of positive Q-criterion (signifying vortices) correspond to the existence of LSB, are coherently embedded within regions of negative Q-criterion, corresponding to shear layers.

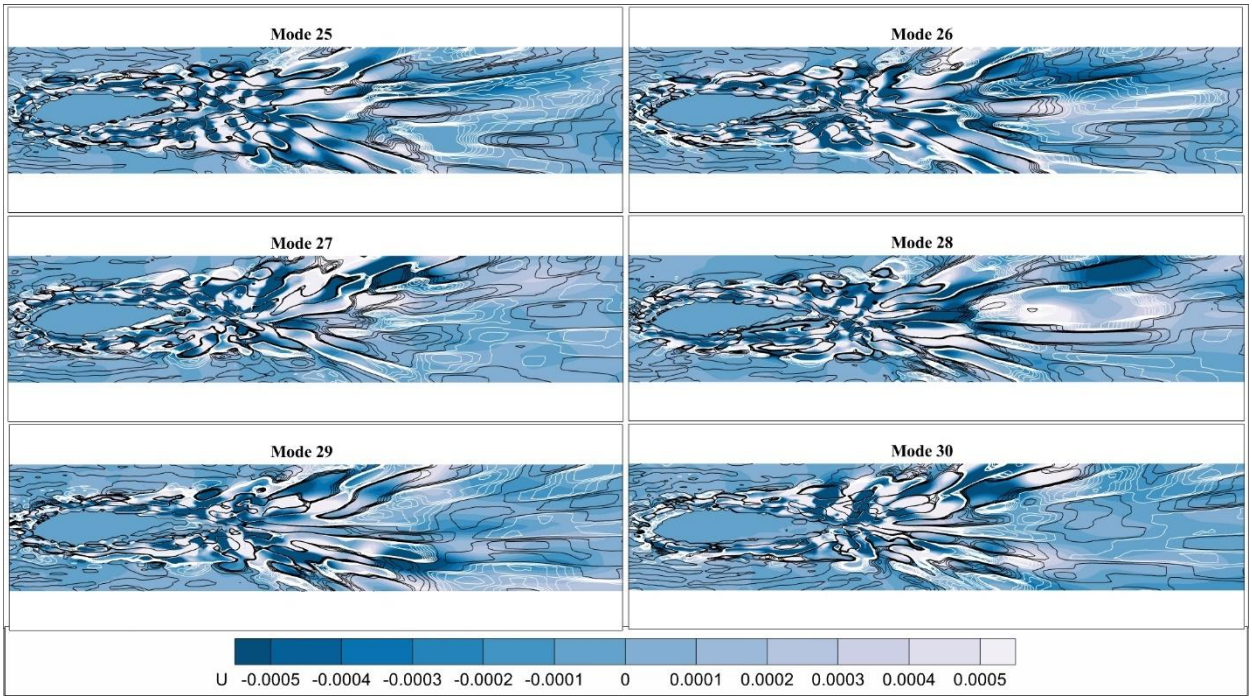

Figure 15 The last six energetic modes. Positive and negative spanwise velocity components are displayed in white and blue respectively, and are overlaid with contours representing streamlines of clockwise and counter clockwise rotation (black and white, respectively).

As vortex structures are advected downstream, corresponding to Mode 2 in Figure 14, their dynamics are significantly influenced by these surrounding shear layers as shown in Figure 14. However, if taking a closer look at the mode 2 in Figure 14, one can discover that the (middle plane) spanwise velocity fluctuations are mild varying from -0.0003 to 0.0002 m/s, signifying that the flow is reasonably well-behaved, where the shear layer (black region) and the vortices are relatively separated. It is also confirmed by contours of Q values in Figure 15. Overall, modes 1 and 2 reduce the flow instability and turbulent intensity, particularly through their effects on the shear layer and the coherence of their vortex structures. Mode 1 primarily captures the large-scale vortex formation near the airfoil's leading edge, where the separation bubble forms and propagates downstream. This dominant structure is critical for initiating the shear layer, which remains highly coherent and stable in this mode. The stability provided by Mode 1

reduces turbulent intensity locally while sustaining large-scale flow organization, which governs the initial phase of energy transfer in the flow field. On the other hand, Mode 2 focuses on the trailing-edge region and the subsequent vortex shedding into the wake. The interaction between the shedding vortices and the downstream shear layer introduces oscillatory forces, which can increase the turbulent intensity and unsteadiness of the flow to a certain level. By analyzing these vorticity pattern, we gain deeper insights into how POD isolates and ranks the flow features according to their energy contributions. For instance, the leading-edge vortex dynamics in Mode 1 are evident in regions of high positive vorticity, while the trailing-edge effects in Mode 2 are associated with more diffused vorticity structures, corresponding to the dissipated, yet coherent vortex structures near trailing edge at the lower pitching angles. Higher-order modes (3-6) capture the fragmented vorticity patterns typical of turbulent shear layers on the surface of the airfoil which correspond to the vortex shedding event and comply with the surface turbulent boundary layer shown in Figure 7c.

In Figure 12, from Modes 3-6, one can observe that as the LEV sheds downstream and detaches, interacted with Trailing Edge Separation Vortices (TESV) as shown in Figure 8c - d and also in the supplementary video, these modes capture the decay of lift and transition to the shedding of Leading-edge Vortex (LEV) and mainly the instabilities near the trailing edge region. The nature of their flow instabilities throughout Modes 3 − 6 in Figure 12 are depicted by the sudden increase in the spanwise velocity component (−0.001 − 0.001m/s). It is further confirmed in Figure 14, where the shear-layer instability becomes more pronounced, as evident in the flow visualizations showing fragmented vortices and increased complexity in the flow field especially around the surface of the wing. To explain it, as the modes progress beyond

Mode 3, the shear layer undergoes further destabilization, with Kelvin-Helmholtz instabilities (Drazin, 1970) dominating the flow dynamics.

These instabilities cause the roll-up and fragmentation of the shear layer, leading to a cascade of smaller vortical structures. This cascading effect is a hallmark of the turbulent energy transfer process (Williams, 2017), where large-scale vorticity lose coherence and transfer their energy to progressively smaller scales during dynamic stall, bursting of LSB and secondary separation (see Figure 7d and Figure 8a to d).

Chapter 4

Dynamic Mode Decomposition

Chapter 4 presents a comparative investigation between standard airfoil and tubercled airfoil by visualizing the three-dimensional vortex dynamics along their corresponding Dynamic Mode Decomposition (DMD) mode. Building on the DMD framework introduced previously, we apply DMD to the same 3D standard airfoil velocity data set—remapped into the body-fixed frame and sampled within the pitching zone ($\pm 0.25\ c$ chordwise, -0.25 c to $1.5\ c$ spanwise)—to extract a library of coherent flow structures associated with dynamic stall. Each DMD mode, ϕ_j, is paired with an eigenvalue, λ_j, whose magnitude and phase encode exponential growth/decay and oscillation frequency, respectively. By overlaying instantaneous vortex fields—visualized via Q-criterion iso-surfaces—with the most energetic DMD modes, we directly compare physical vortex features (e.g., leading-edge vortex roll-up, shear-layer instabilities, and laminar-separation-bubble bursting) to their modal reconstructions. This juxtaposition reveals which modes capture key unsteady phenomena and how they evolve through the pitching cycle. To quantify modal importance, we rank modes by their real parts of $\frac{\lambda_j}{2\pi}$, thereby constructing a growth/decay spectrum that highlights dominant instabilities and transient behaviours. Modes exhibiting positive growth rates correspond to vortex amplification and burst events, whereas decaying modes reflect wake dissipation and vortex shedding attenuation. The resulting spectrum provides a concise, reduced-order map of dynamic stall physics, guiding targeted flow-control strategies. The remainder of this chapter details the

mode–vortex comparisons, spectrum construction methodology, and implications for understanding and manipulating unsteady aerodynamic loads.

Mathematical Model:

In our study, $x_k \in R_n$ denotes a column vector containing information about the discretized flow field (e.g., velocity or vorticity) at time t_k, for $k = 1, 2, \ldots$. Now, it is required to form the two snapshot matrices:

$$X = [x_1, x_2, \ldots, x_{m-1}], \qquad X' = [x_2, x_3, \ldots, x_m].$$

DMD seeks a best-fit linear operator A such that

$$X' \approx A X$$

Direct computation of $A \in R^{n \times n}$ is computational expensive for large n. Instead, we perform a rank-r truncated singular value decomposition (SVD) of X:

$$X = U_r \Sigma_r V_r^*$$

$$U_r \in R^{n \times r}, \Sigma_r \in R^{(r \times r)}, V_r \in R^{(m-1) \times r}$$

We project A onto the subspace spanned by Ur to form the reduced operator:

$$A\tilde{A} = U_r^* X' V_r \Sigma^{-1}$$

$$r \in R^{r \times r}$$

The next step involves computation of the eigenvalues and eigen modes:

$$A\tilde{A} W = W\Lambda, \qquad \Lambda = diag(\lambda_1, \ldots, \lambda_r)$$

where λ_j are the DMD eigenvalues. The corresponding high-dimensional DMD modes are:

$$\Phi \;=\; X' V_r\, \Sigma_r^{-1}\, W \;=\; [\varphi_1, \ldots, \varphi_r].$$

Each mode φ_j evolves in time as:

$$\varphi_j \; exp(\omega_j t), \qquad \omega_j \;= \frac{log(\lambda_j)}{2\pi}$$

Results and Discussion:

Vortex Dynamics:

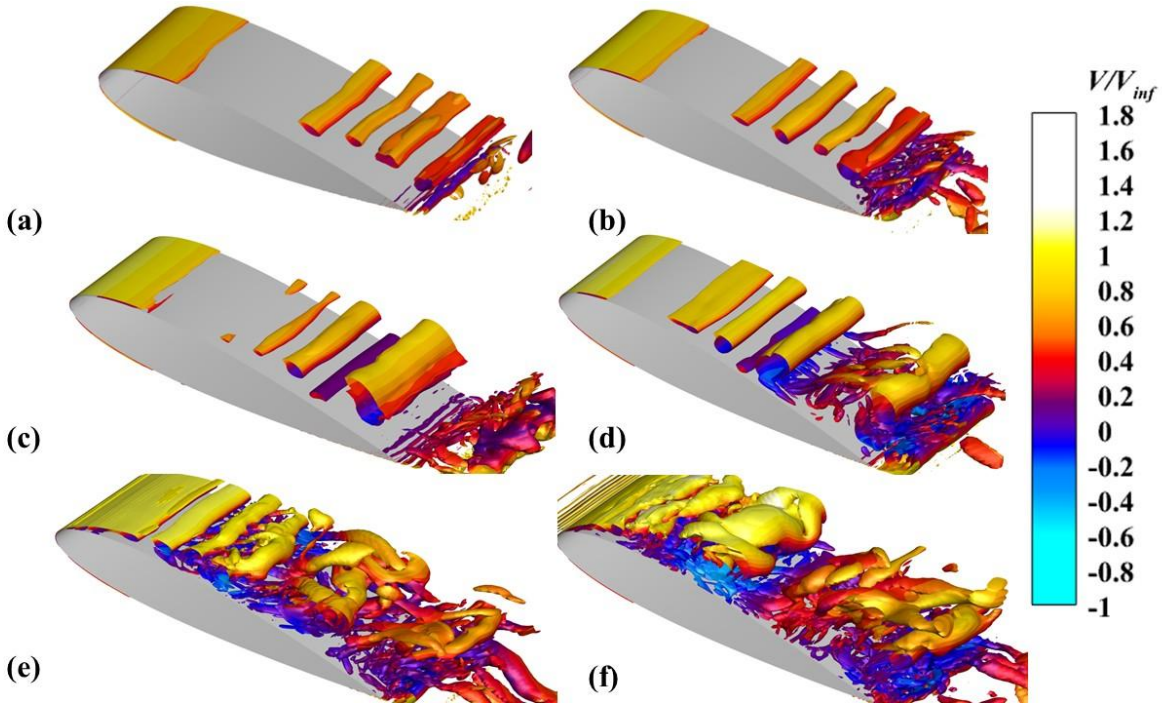

Figure 16 so-surfaces of Q = 5000 (colored by V /V_∞) around the plain wing at t/τ = (a) 0.600, (b) 0.620, (c) 0.640, (d) 0.670, (e) 0.710, (f)0.750.

The behavior of vortex structures around a standard pitching airfoil is a critical determinant of its aerodynamic performance, measured in terms of force coefficients (see Figure 18), and the dynamic stall conditions. Figure 16 shows the formation, transition, and

dynamics of coherent flow structures at different stages of the pitching motion of the plain wing. At the very beginning of the pitching cycle, the trailing edge vortices remain relatively stable, with minor span-wise disturbances localized near the wake region (see Figure 16a). We observe a spanwise instability in the TEV at α =10.46◦ when the wing continues pitching up (see Figure 16b-d). The instability further grows and travels upstream while the wing still undergoes its upstroke for aα ≤ 18.4◦. Beyond a critical threshold, lying between 17.5◦ ≤ α ≥ 18◦ in Figure 16e, this instability triggers a cascading effect similar to a "domino effect", where the initially coherent vortex system collapses into irregular turbulent structures, as depicted in Figure 16f. This process is particularly significant in the dynamic stall phenomenon, as the loss of coherence in vortices amplifies fluctuations in unsteady loads and aerodynamic hysteresis, which are challenging to predict using conventional modeling approaches. Now, Figure 17 exhibits the vortex dynamics around the wing with tubercle on its leading edge at the same pitching angles used for the plain wing shown in Figure 16. The iso-surfaces of Q values (Figure 17a-b) reveal the early development of a laminar separation bubble (LSB) anchored near the trough regions of the tubercled leading edge. At $t/\tau = 0.60$), the flow begins to separate from the surface of the wing just downstream of the trough, creating a small recirculation zone that remains locally attached that indicates a classic LSB. Notably, this separation reattaches further along the trough, indicating a contained bubble rather than a full-span stall. The separation bubble remains confined to the trough between the peak region of the tubercle, rather than spreading across the entire span. The adverse pressure gradient to allow an earlier flow reversal in the trough region. Meanwhile, flow region behind the neighboring peak of the tubercle still sustain attached flow at this phase, avoiding an immediate leading-edge stall. Such

behavior agrees with prior observations that leading-edge separation initiates at the troughs while other spanwise locations remain attached until the wing goes to higher overall angles-of-attack (Hansen, 2012). The result is a delayed and slower onset of stall for the tubercled wing, as the initial breakdown of the flow is limited to isolated LSBs instead of a uniform spanwise separation (t/τ = 0.62).

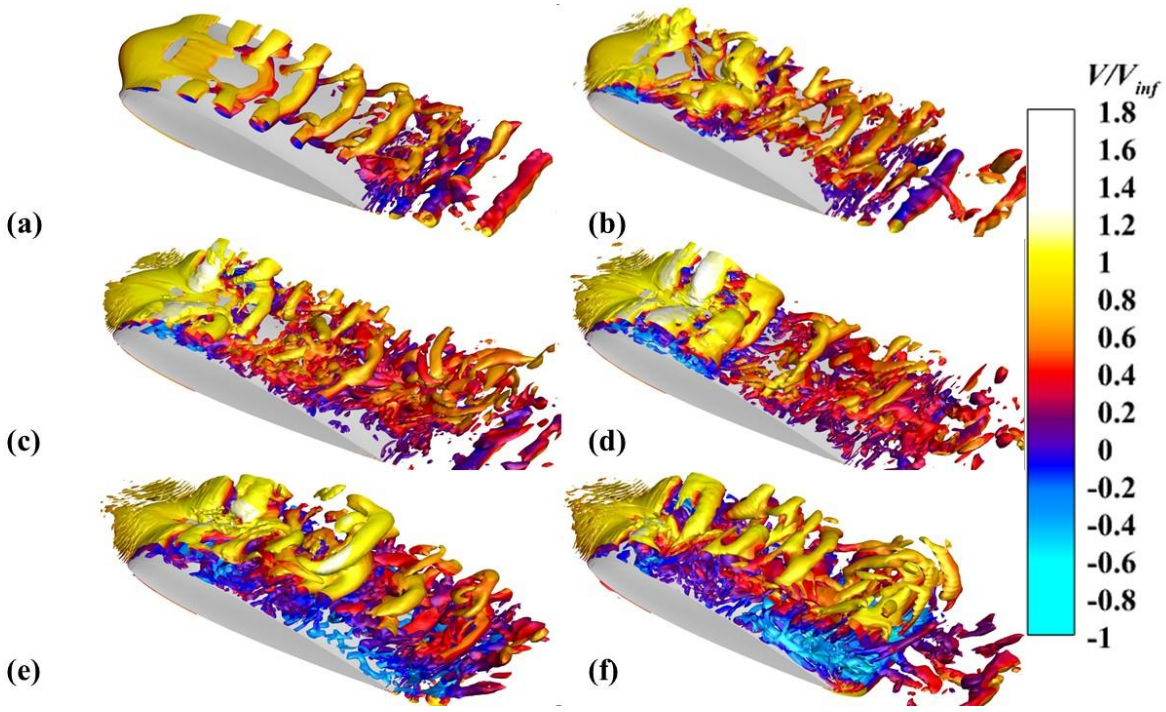

Figure 17 so-surfaces of Q = 5000 (colored by V /V_∞) around the tubercled wing at t/τ = (a) 0.600, (b) 0.620, (c) 0.640, (d) 0.670, (e) 0.710, (f)0.750

At a high Re of 160, 000, the presence and evolution of a LSB play a vital role in controlling the pressure distribution over the surface of a wing (Spalart, 2009). It is important to point out that positive and negative values of friction coefficient (C_f) highlight the regions on the wings with flow attached to it and detached from it, respectively (Figure 19). The growth of the instability from the trailing part of the wing strongly influences the flow behavior at its leading part (Miotto, 2022). We explain different stages in this process using contour plots of

the pressure coefficient, denoted as Cp (Figure 21) and Q values (see Figure 16) around the wing in the mid-plane of the flow field. During the initial phase of the pitching motion ($t/\tau = 0.600 - 0.670$), as shown in Figure 16a-d, the LSB remains attached to the leading edge, maintaining a high pressure difference between the upper and lower surfaces due to the sustained attachment of the boundary layer (Figure 21a-b). However, as α increases beyond approximately $18.4^\circ - 18.9^\circ$ (Figure 16e), the pre-burst of LSB occurs. Here, the LSB starts getting detached from the leading edge of the surface. These phenomena are exhibited in Figure 19a as well in Figure 21c through a less coherent low-pressure zone as compared to that in Figure 21b. For the stall angle of 19° at $t/\tau = 0.75$, the LSB undergoes a sudden burst, triggering dynamic stall. This phenomenon occurs because, beyond a critical angle-of-attack (19° in this case), the vortical structures lose coherence, as shown in Figure 16f, failing to follow a stable convective trajectory along the surface of the blade.

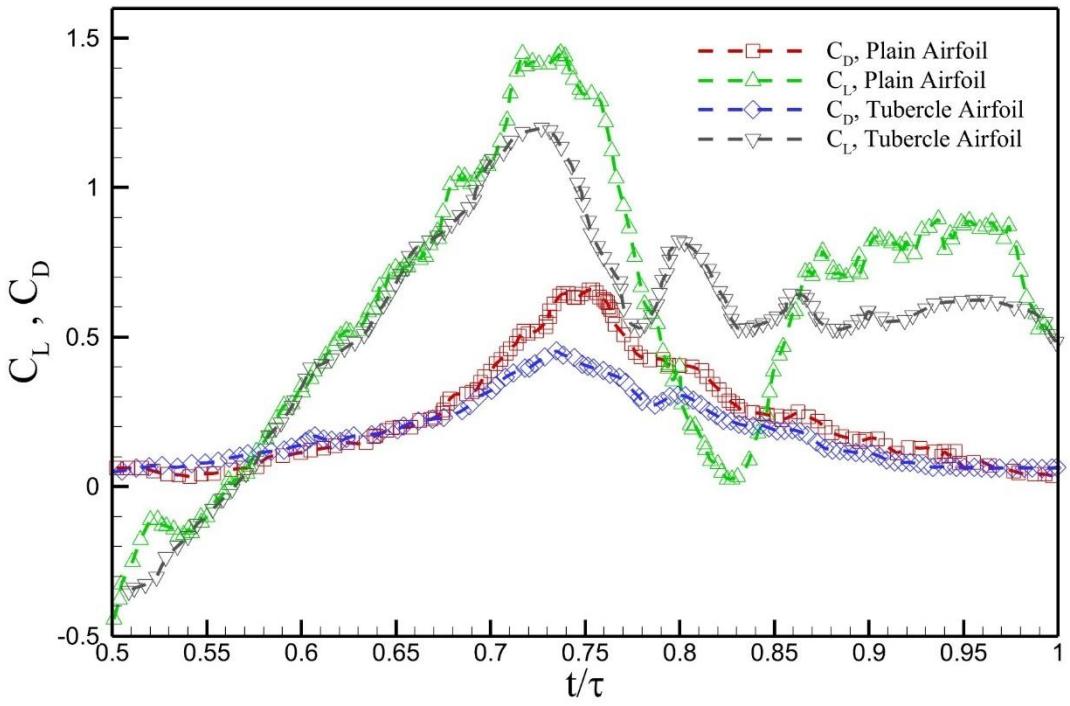

Figure 18 Force Coefficient Comparison between Standard and Tubercle Airfoils from the Last Oscillation Cycle

Consequently, the flow around the wing becomes highly chaotic, leading to unstructured turbulence all along the surface and causing abrupt aerodynamic force fluctuations and breakdown of lift. This development of dynamic stall is further validated by the data presented in Figure 19, where the travel of DSV is traced by the negative value of C_f, depicting the regions of flow separation. The plots of C_f in Figure 19 and Figure 20 is plotted at four-equally spaced locations in the spanwise direction from $x/c = 0$ to $x/c = 0.5$. At t/τ = 0.71 in Fig. 11a, the flow around the surface of the tubercle wing starts detaching from the trailing edge until $y/c = 0.5$, yet not to extent where stall could happen. It is because the LSB are able to maintain its coherence at the leading edge, and thereby this stage indicates only the onset of stall. At t/τ = 0.75, after the Kelvin-Helmholtz instability approaches the leading edge (Rowley,

2009), the LSB bursts and forms a DSV shown in Figure 16f. Subsequently, it travels towards the trailing edge of the wing. The region of flow separation exhibited in Figure 19b traverses towards the leading edge as the DSV moves to the trailing edge.

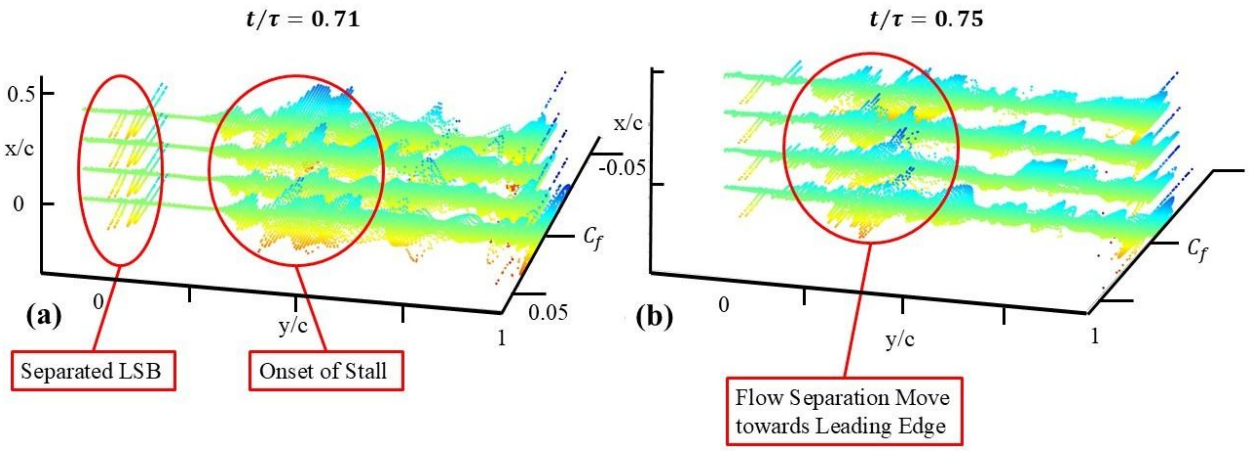

Figure 19 Plots of C_f on different sections of the plain wing at t/τ = (a) 0.710, the onset of stall and (b) 0.750, full stall

As the pitch motion continues (t/τ = 0.67, Figure 17c-d), the LSB in each trough regions begin to feed vorticity into the flow. The plots for Q highlight the formation of distinct streamwise-oriented vortices emanating from the trough regions. These vortices appear as finger-like tubes of swirling flows that stretch downstream along the chord. The spanwise variation in the geometry of the leading edge of the wing, i.e., from peaks to troughs or vice versa, induces a non-uniform pressure distribution. It means that the capacity of wing to produce lift varies spanwise direction. This resulting gradient in circulation of the flow serves as the source of the observed counter-rotating vortex pairs (CVRPs) in each trough (Hand, 2017). It appears that each trough of a tubercle behaves like a small separated wingtip, rolling up the shear layer into a longitudinal vortex. The sinusoidal leading edge thus passively localizes the separation and converts a large continuous shear layer into a series of discrete vortical structures. Visualization from experiments by Hansen et al. (Hansen, 2012) showed the same

phenomenon. Here, streamwise vortices consistently formed in the troughs between tubercles remain to entrain the higher-momentum fluid from outside the boundary layer and mix it into the separated region. This mechanism effectively energizes the LSB and delays its burst. In our simulations, the vortices in the trough region grow and become stronger at by t/τ = 0.71, where higher vorticity core is indicated by more intense iso-surfaces of Q. Yet, these flow structures remain well-organized and distinct, marking a 3D vortex topology passively controlled by the geometry of tubercles

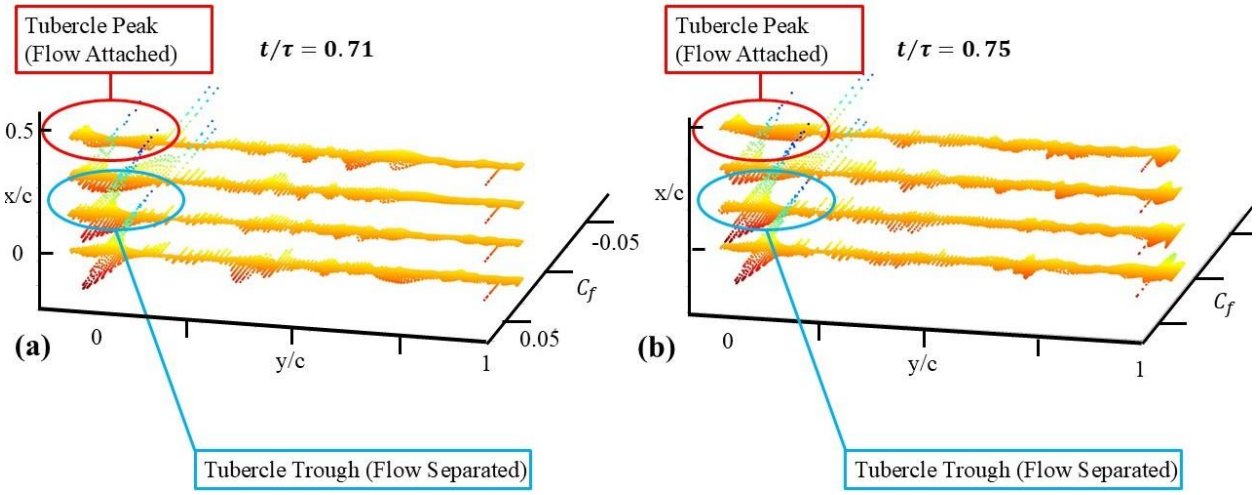

Figure 20 Plots of C_f on different sections of the tubercled wing at t/τ = (a) 0.710, the onset of stall and (b) 0.750, full stall

At later instants (t/τ = 0.71 − 0.75, Figure 17e-f), the vortices, originating from the trough regions amplify and begin to lose coherence as the wing approaches its peak amplitude in the pitch-up cycle. The vortex activity intensifies with the increasing angle-of-attack, and their core circulation and vorticity grow larger with time. It is also the time when these vortices e.g. CRVPs appear stronger and start interacting with each other and with the airflow off the surface shown in Figure 17e. It could possibly be an implication of the interaction between the counter-rotating vortex pair and reserve counter-rotating vortex pairs (RCRVP) (Zhao M. a., 2021), which

is shown in Figure 17e. Notably, the initially smooth vortical tubes become distorted and secondary vortex structures emerge alongside them. By $t/\tau = 0.75$, these secondary counter-rotating eddies are visibly entwined with the primary vortices, which is a sign of the organized vortex tubes breaking down. The onset of this breakdown coincides with the formation of a larger-scale leading-edge vortex that begins to detach to effectively act as the DSV. In contrast to the development of dynamic stall process of a plain wing, (see Figure 16e-f), where a single massive DSV forms abruptly, and the tubercled wing experiences a more distributed vorticity field. The previous discrete vortices convert into smaller structures and soften the stall process (Zhao M. a., 2023). We also observe an indication for this behavior in Figure 18.

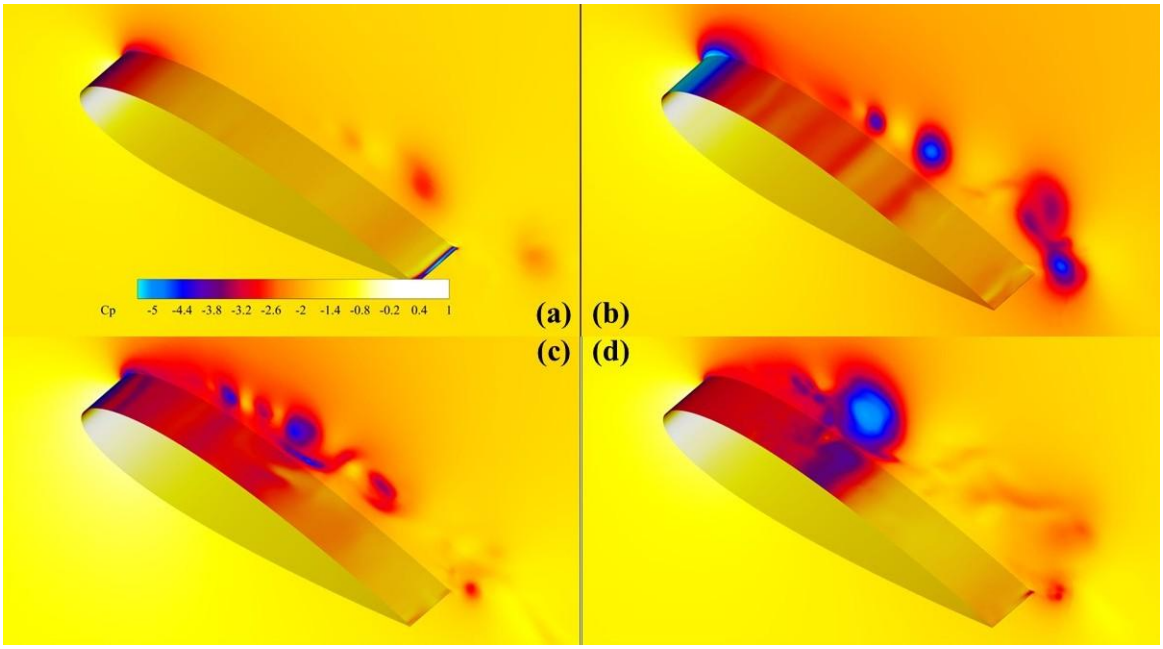

Figure 21 Contours for pressure coefficient varied from -5 (Blue) to 1 (White) on mid-plane (x/c = 0.5) and around the plain wing at t/τ = (a) 0.640, (b) 0.670, (c) 0.710, and (d) 0.750

This situation demonstrates a DSV remaining closer to the surface for longer and getting shed later in the pitching cycle, rather than shedding rapidly away (Zhao M. a., 2023). Throughout the pitching cycle of the tubercled wing, the simulations highlight a pronounced

spanwise variation in the flow attachment, which is especially evident in the distribution of CP between t/τ = 0.71 − 0.75. Contours of C_P on the slices at the peak of the tubercle (Figure 22a and c) versus the ones at a trough (Figure 22b and d) show two distinct behaviors. At t/τ = 0.71 (onset of stall), the peak region maintains a strong suction on the wing's leading edge that is a signature of an attached or only mildly separated flow. Contrarily, the trough region at the same time exhibits a much flatter distribution of C_P. The suction zone is greatly diminished or absent, and there may even be a plateau in C_P in the forward portion of the chord. It is classic evidence of the LSB with reattachment or an early separated flow. At the same instants, the spanwise distributions of Cf further highlight the stall mitigation, offered by the tubercles. At t/τ = 0.71 for the tubercled wing (Figure 22), the peak locations still exhibit positive pressure coefficient, indicating the attached flow. By t/τ = 0.75, when dynamic stall is imminent, contours on the slice at the trough show complete separation of the flow, and CP remains nearly constant or slightly positive over most of the chord. It confirms a stalled condition. Contours on the slice at the peak of the tubercle at the later time also show loss of the sharp suction zone, but it still indicates more suction than the trough. It suggests that the flow around the peak of the tubercle contributes less towards the stall than the troughs. The spanwise phase lag in stall is what gives the tubercled wing its extended lift curve and more gradual stall, which explains that not all sections of the wing lose lift at once3. In a previous study by Hansen et al. (Hansen, 2012) and Lee et al. (Lee, 2004), measurements of pressure on a wing's surface showed that separation/reattachment regions stayed confined to troughs up to higher angles, yielding significant spanwise differences in distributions of lift and pressure over the wing.

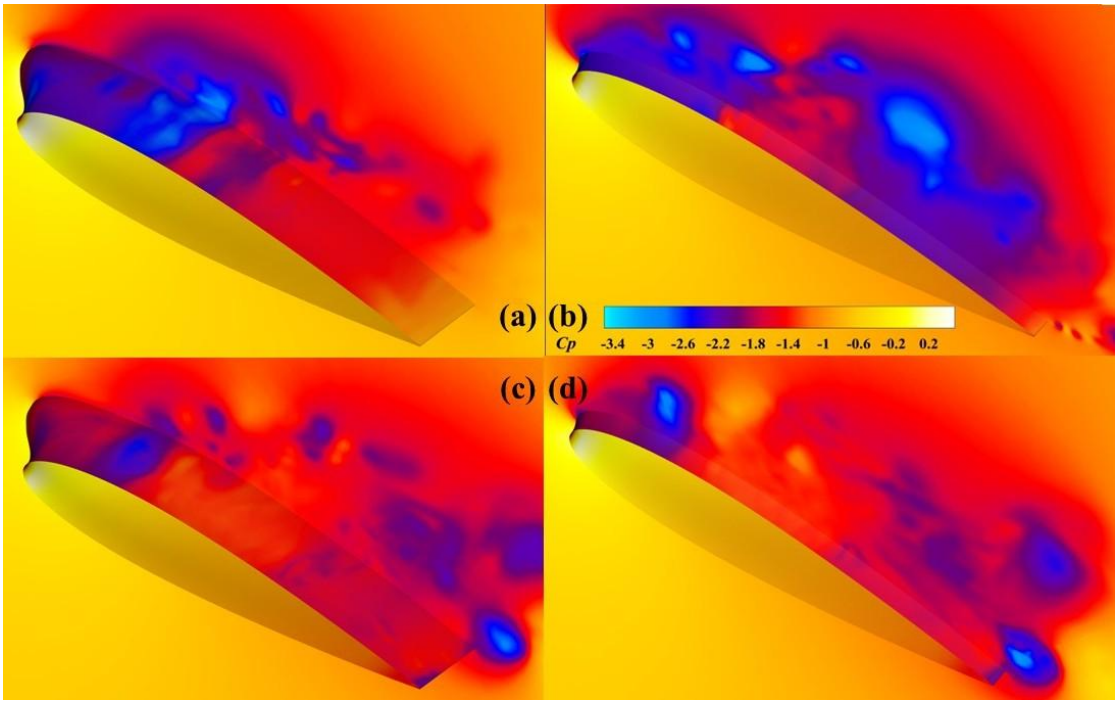

Figure 22 Contours for pressure coefficient varied from -3.4 (Blue) to 0.5 (White) on mid-plane (x/c = 0.5) (a)&(c) and on quarter-plane (x/c = 0.25) (b)&(d) of the tubercled wing at t/τ = 0.710 (a)&(c), 0.750 (b)&(d)

Dynamic Mode Decomposition-Based Analysis:

Dynamic Mode Decomposition is a fully data-driven technique that extracts spatio-temporal coherent structures from time-resolved flow fields by approximating the action of the Koopman operator on observables. Unlike classical modal decomposition techniques, e.g., POD, which organize modes by energy content alone, DMD yields modes each associated with a single complex eigenvalue, whose magnitude encodes exponential (Takemura, 2004) growth/decay and whose argument gives the oscillation frequency. This property makes DMD particularly powerful for uncovering instability mechanisms, resonant oscillations, and nonlinear interactions in unsteady aerodynamic flows, such as the dynamic stall vortices that develop on a pitching wing. The resulting DMD modes cleanly separate the dynamic stall vortex (at the pitching frequency), the post-stall wake shedding (at its own frequency), and higher-

harmonic or nonlinear interaction modes. These modal features, including growth rates, shedding frequencies, and spatial foot- prints, form the basis for reduced-order models, active or passive flow control strategies, and deeper physical understanding of how pitching wings and blades interact with unsteady flows.

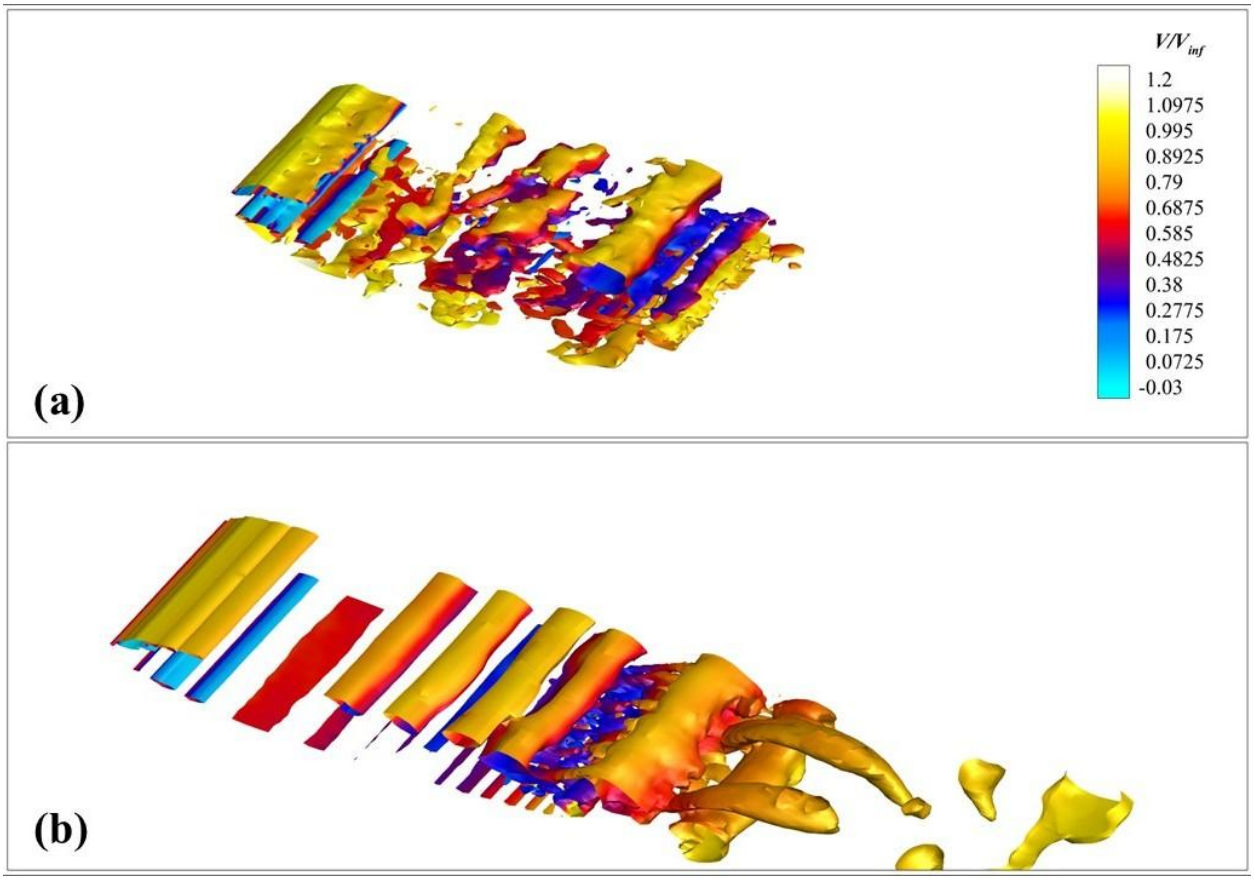

Figure 23 a) Reconstruction of the flow around the plain wing using modes, containing up to 90% of energy with plots of iso-surfaces of Q = 4500 colored by V /V_∞ and (b) the original Flow from DES at t/τ = 0.58

To ensure that we capture the majority of the flow physics, we now reconstruct the flow by extracting the high-energy mode at the associated timestep and plotted up to 90% of kinetic energy for both plain and tubercled wing in Figure 23 and Figure 24, respectively. Figure 25 and Figure 26 present how each mode picks out specific coherent structures for plain and tubercled wings, respectively. For instance, Mode 1 (Figure 25a) contains the steady separation bubble

near the leading edge, whereas Mode 4 (Figure 25c) contains a large vortex structure shedding along the wing. The ability of DMD to extract such meaningful structures related to dynamic stall were not demonstrated in literature previously. In our case, the DMD modes cleanly separate the low-frequency and high-frequency contents of the flow, much like the decomposition reported by Kern et al. (Kern, 2024)for laminar separation bubbles.

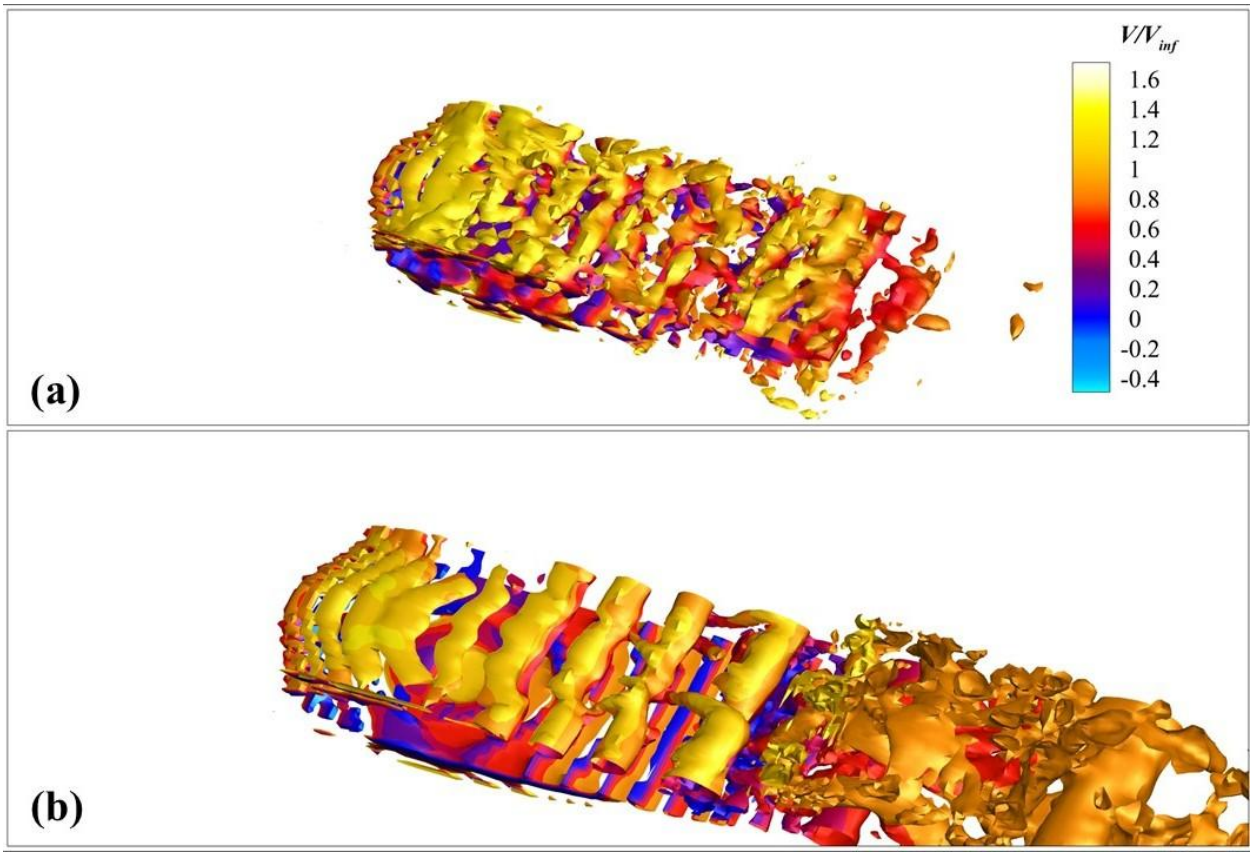

Figure 24 a) Reconstruction of the flow around the tubercled wing using modes, containing up to 90% of energy with plots of iso-surfaces of Q = 4500 colored by V/V_∞ and (b) the original Flow from DES at $t/\tau = 0.58$

Mode 2 is a low-frequency mode that captures primary vortex shredding event and the initial roll-up of a vortex at the leading edge. In Figure 25b, Mode 2 features a concentration of vorticity in the leading-edge region, coincident with where the LSB forms and bursts. The low Strouhal number (St = 0.0351) indicates a period much longer than the convective time over the

wing. It corresponds to the slow variation or pulsation of the separation bubble.

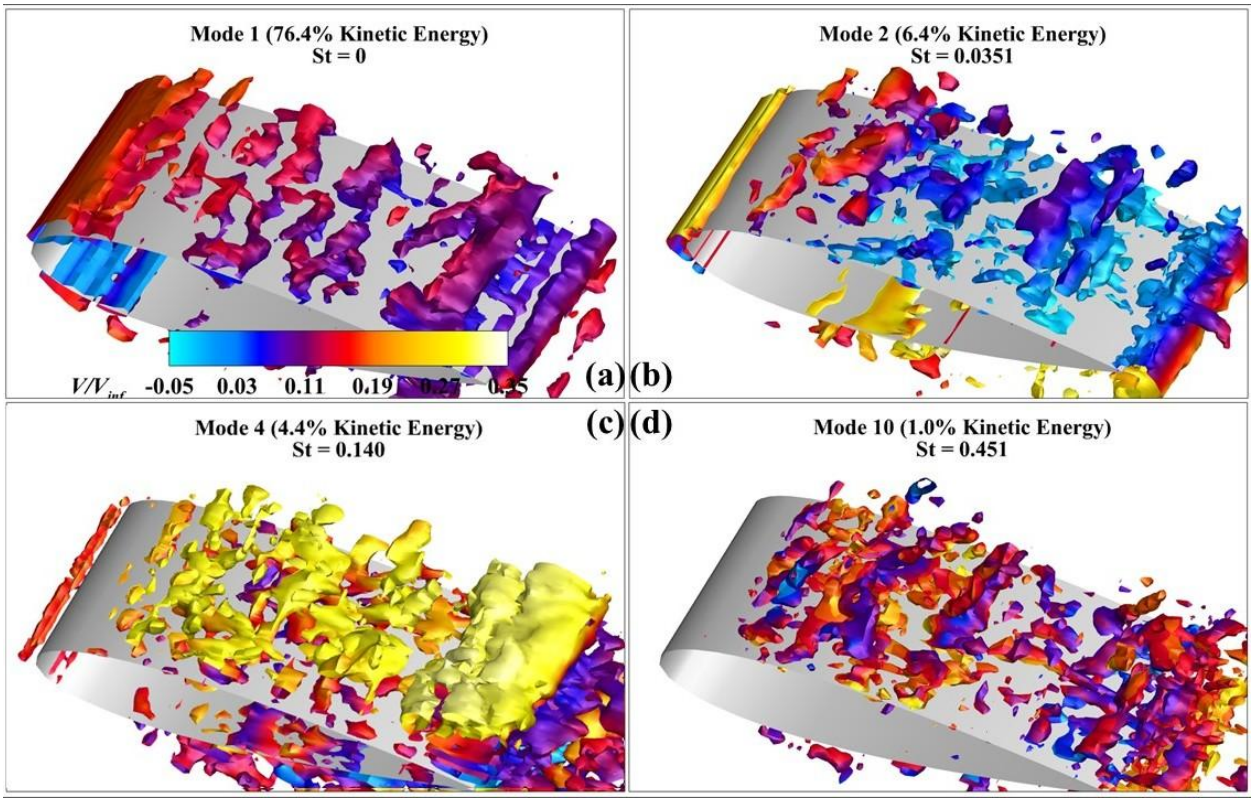

Figure 25 The strongest DMD modes for the flow around the plain wing using the iso-surfaces of Q = 7000 colored by V/V_∞

Physically, Mode 2 can be interpreted as the bubble breathing mode, where the LSB slowly enlarges and then rapidly gets shed as a vortex. It aligns with observations of a low-frequency oscillation in LSBs in prior studies by Takemura et al (Takemura, 2004) Earlier, direct numerical simulations (DNS) from Kern et al. (Kern, 2024) determined that LSBs exhibited a low-frequency flapping (on the order of $10^{-2} - 10^{-1}$ of Strouhal Number(St)) associated with its growth and bursting, in addition to the faster instabilities within the shear layer. The presently determined mode 2 embodies that same phenomenon during dynamic stall. It shows the bubble growing in the region of the leading edge and the trailing edge of the standard airfoil (more coherent structure in Figure 25b) and then shedding near the surface of the standard airfoil with minor

bursting (more scattered vortex structure in Figure 25b). It is important to mention that it is the first step in the formation of the LEV. Notably, mode 2 contains about 6.4% of the flow energy, making it the second-most energetic mode. It highlights that the LSB's formation and bursting is a dominant unsteady phenomenon for this high-Re pitching wing. In the temporal snapshots, the effect of mode 2 is visible around $t/\tau = 0.67{\sim}0.71$ (see Figure 16d–e), where the bubble is unsteady and about to be shed as a vortex. Besides, mode 4 corresponds to the formation and convection of the DSV across the wing. Its frequency (St = 0.141) is associated with the main vortex shedding event. The spatial structure in Fig. 15c shows a large-scale vortex spanning from the leading edge to beyond the mid chord region over the upper surface, which is precisely the footprint of the DSV. This mode essentially captures the LEV/DSV as it travels from the leading edge to the trailing edge. The mode shape has a significant amplitude over the wing's chord, indicating the influence of the shedding vortex on the flow field and the induced suction over the wing as it passes over it. It contains about 4.4% of the energy, which is significant for a single oscillatory mode and underscores the importance of the DSV in the unsteady aerodynamics. We can relate mode 4 to the distinct shedding of the stall vortex observed in the simulation. For instance, St = 0.141 roughly corresponds to the inverse of the time it takes the vortex to dissipate along the chord (on the order of 7 chord lengths per cycle). During $t/\tau = 0.71{\sim}0.75$ (Figure 16d–e), the DSV is fully active, and mode 4 is the manifestation of the large coherent vortex structure dominating the flow. Previously, numerical studies from Visbal et al.9 and Wen et al.48 showed that once the shear layer rolled up into a vortex during stall), that vortex was travelling downstream and caused peak loads before shedding. When we introduce the leading-edge protuberance, the DMD mode shape of each

flow phenomenon gets altered, as presented in Figure 26. Specifically, mode 1 contains the majority of the kinetic energy from the flow field and corresponds to the near-steady or slowly varying component of the flow. It essentially represents the time-averaged flow field (or very low-frequency content). The iso-surface plots of Q for mode 1 shows a large recirculation region over the airfoil, which is the footprint of the LSB and the separated flow. This mode captures the long-lasting flow features, such as the presence of the LSB prior to stall and carried over until the trailing edge. Physically, mode 1 can be seen as the base flow around which the unsteady events occur, e.g., the maintained separation bubble and shear layer. A similar leading low-frequency/zero-frequency mode was noticed in other DMD-based analyses of stalled flows, essentially representing the mean separation bubble structure49. Mode 2 is a distinctly higher-frequency mode that captures rapid vortex shedding in the shear layer as the LSB transitions to turbulence. Its St = 0.45 corresponds to the characteristic frequency of Kelvin–Helmholtz (K–H) instability rolls in the separated shear layer. In the iso-surface plot of Q for mode 2, we observe fine-scale vortical structures concentrated near the leading edge and along the shear layer downstream. It reflects the periodic roll-up and shedding of vortex structures from the bubble. Physically, mode 2 represents the mechanism bursting of the LSB. As the bubble becomes unstable, it sheds a train of small vortex structures at a high frequency (Takemura, 2004). These shed vortices are shed downstream rapidly, and their accumulation leads to the formation of a larger LEV. Such high-frequency content and scattered spatial structure, concentrated along the shear layer, hints towards its association with the instability of the shear-layer and vortex shedding that precedes and accompanies the bubble's collapse. Notably, our finding aligns with recent DNS-based results by Kern et al. (Kern, 2024) who

observed strong coherent vortex shedding from the LSB just before the DSV is formed.

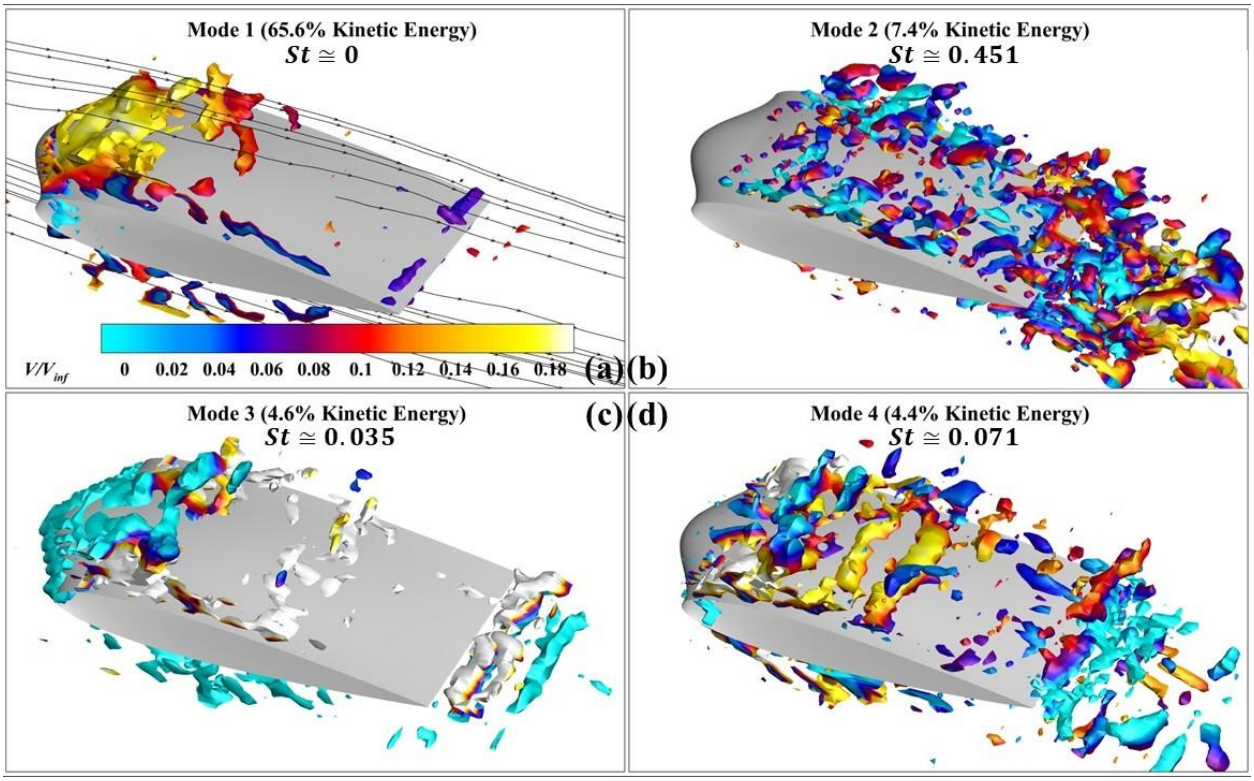

Figure 26 The strongest DMD modes for the flow around the plain wing using the iso-surfaces of Q = 7000 colored by V/V_∞

Mode 3 is a low-frequency mode with an order of magnitude significantly lower in St than mode 2. Its St = 0.0351 is of the order of the pitching frequency or the slow flow-shedding oscillations of the separated flow. The spatial structure of mode 3 shown in Figure 26c exhibits change in the large-scale flow, such as broad regions of vorticity above the wing that span from the leading edge through mid-chord. It suggests that mode 3 is connected with the evolution of the global flow at stall, particularly the flow's slow progression from being attached to getting fully separated, and to subsequent reattachment. We interpret mode 3 as the one capturing the attachment/reattachment dynamics around the maximum angle-of-attack. When the wing reached α◦ during the upstroke, the flow slowly loses attachment, leading-edge suction is reduced, and the LSB expands. During the downstroke, the flow slowly reattaches. These are

relatively low-frequency events compared to the K–H shedding. Indeed, prior studies by Zaman et al. (Zaman, 1988) noted that laminar separation bubbles and stalled flows exhibited a distinct low-frequency unsteadiness, often termed “bubble breathing” or a flow oscillation, that involves the growing bubble and shrinking on timescales much longer than the shear-layer shedding. Additionally, mode 4 has a Strouhal number in between pitching frequency and the one associated with the bursting of LSB and the shedding frequency. This observation places it in an intermediate range of unsteadiness. The low St of mode 3 and its large spatial extent, covering the wing’s leading region, mirror the very slow global variations in the flow. This mode’s contribution to unsteady forces would manifest as a slow oscillation in lift and moment as the airfoil enters and exits stall.

The iso-surface plots of Q for mode 4 reveal flow structures of intermediate size, particularly in region starting from the mid-chord to the trailing edge of the wing. We associate mode 4 with the detachment and convection of the large vortex structures, as well as the unsteady dynamics of the trailing-edge flow. In essence, mode 4 appears to capture the process of the LEV rolling back over the wing and the formation of the trailing-edge vortex. These events are faster than the global stall/reattachment (mode 3) but slower than the shear-layer eddies (mode 2). For example, once the LEV/LSB forms in in the trough, it sheds downstream over a fraction of the pitching cycle to form counter rotating vortex pairs (RCVRP) (Zhao M. a., 2021). In our context, it represents the gradual loss of leading-edge suction and bubble elongation as stall sets in. It also hints for the gradual recovery of flow attachment after the stall during the downstroke. Additionally, the interaction between the LEV and the trailing-edge flow, such as the shedding of the TEV or the oscillatory separation at the trailing edge, likely

occurs at this intermediate timescale. Prior modal analyses of dynamic stall flows (Dunne, 2016) found modes corresponding to the convection of the stall vortex and its effect on the wing's aft region, often at a frequency of the order of the itching frequency or its first harmonic. Mode 4 aligns with those findings that St = 0.071 is roughly twice that of mode 3, implying it might be related to the first harmonic of the fundamental stall oscillation. Physically, this mode may describe the coherent motion of the LEV/TEV system in trough area, and grow into RCRVP. For instance, the wing experiences unsteady loads when the LEV is halfway along the chord (moment stall) and as the TEV forms at the trailing edge.

Comparison Between Flow Dynamics and the Modes:

The DMD mode corresponding to zero frequency (St = 0) represents the essentially steady or time-averaged flow structure during the pitching motion. For the plain airfoil, this mode depicts a large separated flow region spreading over the wing's suction surface as α increases. In dynamic stall conditions at moderate Reynolds number, the baseline flow typically features a broad separation that originates near the leading edge and extends towards the trailing edge, especially once stall is initiated. In contrast, a base-flow mode of the tubercled wing shows a distinctly different pattern, in which the separated flow is broken up into "tall cells", which are potentially alternated patches of separated and attached flows along the span, dictated by the peaks and troughs of a tubercle (Hansen, 2012). The leading-edge tubercles produce counter-rotating stream- wise vortex pairs that energize the boundary layer behind each of its peak, maintaining partial attachment in those regions while separation is confined primarily to the trough regions (Benton, 2019). As the plain airfoil pitches towards stall, a small LSB typically forms near the leading edge due to low separation and reattachment in the

laminar regime. At Re = 160, 000, this LSB can persist up to a certain angle, after which it bursts suddenly, transitioning the flow to turbulence and feeding vorticity into a newly forming leading-edge vortex. This process is a known precursor to dynamic stall at transitional Reynolds numbers. When the LSB bursts, the shear layer rolls up into a coherent leading-edge vortex, marking the onset of the formation process of LSB54. In the DMD spectrum for the plain wing in Figure 26, a low-frequency mode (St = 0.140) emerges that is associated with this global flow reorganization. It captures the moment when the eruption of LSB and roll-up of LEV occur. Physically, this mode represents the rapid destabilization of the separated shear layer and the birth of the DSV. Its low Strouhal number reflects the long-time scale of the event which is of the order of the pitching period itself. It indicates onset of a single large-scale stall per cycle. The tubercled wing, however, alters this scenario.

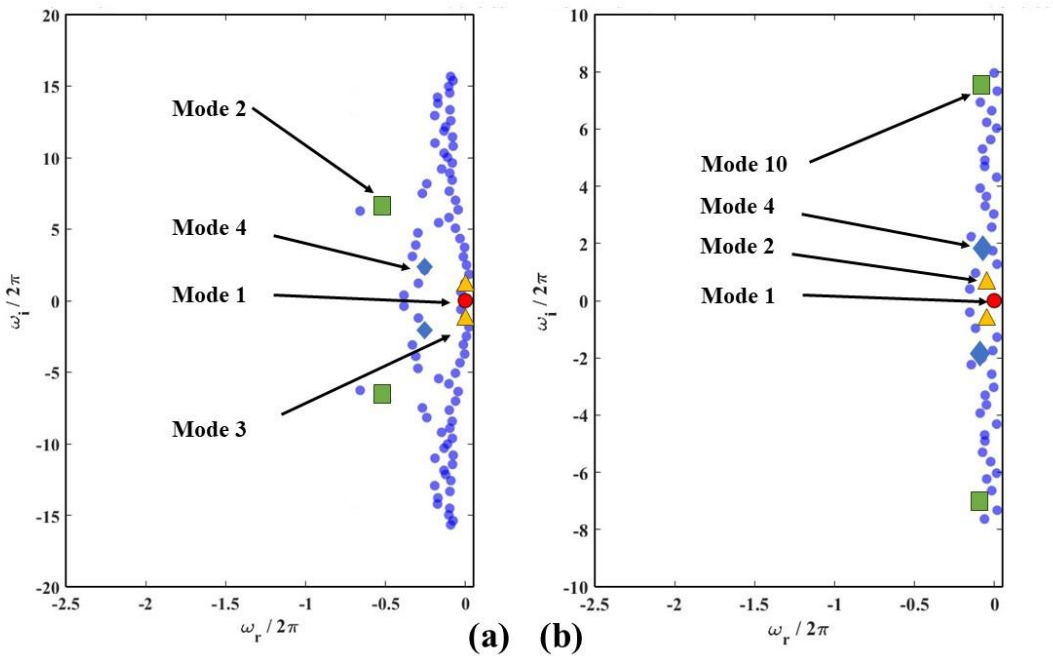

Figure 27 Real and imaginary components of the angular frequencies for the (a) tubercled wing (b) the plain wing

The presence of tubercles delays and softens the roll-up of the leading-edge shear layer.

According to Figure 27, instead of a single abrupt bubble burst spanning the entire wing slowly, each trough may foster a smaller separation bubble that tends to burst at a greater dissipation rate or at slightly different times across the span. Moreover, the tubercle-induced streamwise vortex structures likely accelerate transition to turbulence in the trough regions. These high-St mode in Figure 26b and d indicate that the unsteadiness in the flow field is dominated not by a single large bubble-bursting event, but by smaller-scale shear-layer disturbances that occur more continuously. Tubercles effectively instill a multi-frequency behavior which is about the energy concentrated in the single LSB. The bursting/LEV-rollup mode for the plain wing is redistributed into higher-frequency content associated with more incremental vortex shedding and reattachment events. Prior investigations on the flows around of tubercled wings by Hansen and Lee (Hansen, 2012) support this interpretation. The tubercles modify the boundary-layer stability and alter the frequency of shear-layer fluctuations, generally shifting energy toward higher-frequency less coherent vortex structures. Introducing leading-edge protuberance dramatically changes the character and energy of the DSV mode. The tubercled wing shows a markedly weaker and less coherent DSV in the higher-order mode (e.g. mode 2 with St = 0.451). Flow visualization and modes indicate that the roll-up of the vorticity sheet is significantly delayed in the case of tubercles in mode 4 (see Figure 26d. By the time a stall vortex forms, it does so farther downstream than in the case of the plain wing6. It is achieved through the action of the counter-rotating streamwise vortices generated at each tubercle8 in which these vortex structures disrupt the spanwise uniformity of the shear layer and siphon away vorticity that would otherwise feed the leading-edge vortex. Notably, the early detachment of the DSV on the tubercled wing is a trade-off, which means the stall vortex does not remain

attached to the suction surface for long, limiting the advantageous lift from a prolonged vortex. But it also prevents the vortex from growing excessively large and causing an abrupt stall (Zhao M. a., 2017). It is reflected in the temporal profiles of the force coefficients in Figure 18. The plain wing gets a larger overshoot in lift due to a strong DSV staying attached for a longer time but then a sharper drop. On the other hand, the tubercled wing has a more modest overshoot and a more gradual decline in lift. The DMD modal energy content supports the perspective that the plain wing concentrates energy in the low-St DSV mode e.g. Modes 2 and 4 in Figure 25b and c, respectively, whereas the tubercled wing distributes energy across multiple modes that can be an indication of no single vortex dominating the dynamics.

Both configurations (Figure 25d and Figure 26b) exhibit higher-frequency modes associated with small-scale shear-layer instabilities, vortex shedding, and wake development, but their prominence differs greatly between the plain and tubercle cases. In the latter stages of dynamic stall on the plain wing, once the main DSV is shed, the separated shear layer over the airfoil (especially toward the trailing half of the chord) becomes susceptible to K-H instabilities. These act as a train of smaller vortex structures shed from the shear layer and trailing edge. The DMD modes for flows around the plain wing at moderate Strouhal numbers (e.g. St $\gg$ 0.2) correspond to these vortex shedding, which essentially is the indication of the breakdown of the large stall vortex and the shedding of subsequent trailing-edge vortex (TEV). However, in this case, these high-frequency modes typically carry relatively low energy compared to the dominant DSV mode as they are a byproduct of the passage of the stall vortex and the onset of fully separated flow. Consequently, it contributes to the turbulent wake but not significantly influencing the lift during the onset of stall. For the tubercled wing, the high-

frequency and fast-dissipating shear-layer modes (Fig. 17a) play a more critical role in the flow dynamics. The tubercles provoke earlier and more vigorous shear-layer instabilities due to the wavy pressure distribution along the leading edge and the alternating attached/separated regions with a higher flow velocity. As a result, vortex structures associated with shear layer instabilities are shed nearly continuously from the trough regions, even before a large-scale stall vortex can develop. These small-scale vortex structures appear in the DMD as strong high-St modes, such as the one with St = 0.451, and are spatially concentrated in the separated shear layers emanating from each trough of the tubercle. Such high-frequency modes rival or even exceed the energy of the low-frequency stall vortex mode, indicating a redistribution of energy to smaller scales but at a fast dissipation rate (Figure 27a). Physically, it means that the flow associated with the tubercled wing is characterized by a richer spectrum of smaller vortex that mix the flow and consume the shear-layer vorticity, rather than having one large vortex. It has an implication for stall dynamics that the continuous shedding of small-scale vortex structures leads to a faster vortex breakdown. Moreover, the presence of these high-frequency modes can interact with the DSV itself. For example, shear-layer vortices forming near mid-chord can influence the trajectory and decay of the DSV. The plain wing follows the classical pattern for bursting of the laminar bubble, a single strong leading-edge vortex forms (low-St mode) causing a dramatic overshoot in lift, and then this vortex gets shed. It leaves behind chaotic small vortex structures (high-St modes) as the wing enters deep stall. Nevertheless, the tubercled wing shows a different modal signature that correlates with mitigation of stall. The tubercles distribute the flow instability into multiple modes, where the base flow separation is broken into cells, the roll-up of LEV is delayed and less synchronized. In addition, the DSV is weaker and

fragmented, and high-frequency shedding is enhanced. It agrees with experimental observations by Badia et al.6 that tubercles “soften the onset of stall” and produce a shorter but milder overshooting lift, as mentioned previously.

Chapter 5

Dynamic Stall under Varying Pitching Conditions

Increasing pitch amplitude and reducing frequency fundamentally alter the coherent structures extracted by DMD and mrDMD, revealing how laminar separation bubbles (LSBs) burst, dynamic stall vortices (DSVs) travel, and leading-edge vortices (LEVs) shed. At low amplitudes and high reduced frequency, DMD modes cluster near the imaginary axis, indicating sustained oscillations locked to the pitching motion. As amplitude grows (15° to 30°) and k decreases (0.3 to 0.1), new modes appear off the imaginary axis: a high-frequency, strongly decaying mode marking LSB bursting; a low-frequency, weakly decaying DSV-travel mode reflecting the shedding stall vortex; and a growing LEV-shedding mode whose positive growth rate signals the rapid vortex roll-up at stall onset. Standard DMD efficiently reconstructs flows dominated by periodic shedding, but in the most non-stationary case (k=0.1, 30°) mrDMD's time-localized decomposition isolates each phase (bubble burst, vortex growth, and shedding), yielding lower reconstruction error. These findings demonstrate that mode shapes not only capture spatial vortex dynamics but also encode their temporal persistence and transitions through dynamic stall.

Results and Discussion:

Modal Shape Analysis (DMD and mrDMD):

The DMD modes highlighted in this figure capture the traveling dynamic stall vortex

(DSV) as it forms, sheds, and decays across different pitching amplitudes (15°–30°) and reduced frequencies (k = 0.1, 0.2, 0.3). Each subplot labels the mode's kinetic-energy fraction (0.40–3.51 %) and Strouhal number (St = 0.053–0.14), indicating how strongly and how often each vortex structure oscillates within the cycle. Lower-St modes (St≈0.035–0.07) with higher energy (2–3 % of KE) show large, coherent vortex cores traveling along the chord, representing the dominant DSV that imparts the main lift overshoot and subsequent breakdown. Intermediate-St modes (St≈0.08–0.09) depict smaller-scale vortices and shear-layer roll-up in the wake, carrying around 1 % of the energy. The highest-St modes (St≈0.11–0.14) are more localized near the trailing edge and decay rapidly, reflecting fine-scale turbulence generated as the DSV sheds. Specifically, as shown in Figure 31b-2, we discovered that DSV mode is not present under the current pitching condition ($k = 0.3, \alpha = 20^{\circ}$), because the stall is delayed as we increase the pitching frequency due the apparent mass effect (Visbal, 2018), postponing separation and allowing the DSV to draw more energy from the mean flow before shedding. This is further proved Figure 31 c, c-1, c-2 and d,d-1,d-2 where in deep stall e.g. $\alpha \geq 25°$, where the decrease in St but stronger magnitude of the X-vorticity, which is caused by the inertial confinement reduces viscous diffusion relative to convective transport, thereby slowing the exponential decay of the DSV mode in the DMD spectrum (McCroskey, 1981).

Additionally, as shown in Figure 30 low-order modes (Mode 2 at St≈0.035) concentrate over the airfoil's suction peak, representing the primary LEV roll-up and conveying most coherent energy. Intermediate St modes (St≈0.06–0.09) depict shear-layer instabilities and secondary vortex shedding, marked by lower energy contributions (~1%) from smaller-scale structures. The gradual decline in mode energy with increasing mode number underscores that

the LEV is one of the most energetically significant but not dominant structures in kinetic-energy terms. Across all k and amplitudes, the clustering of St values around 0.05–0.10 aligns with classical dynamic-stall vortex frequencies for pitching airfoils at $Re \approx 10^5$. Additionally, it is general trend that from a to a-2, b to b-2 and c to c-2, as pitching frequencies (k) increases, the LEV forms later but with greater suction (Tsang, 2008). Therefore, the Strouhal number of LEV mode across all pitching frequencies are showing the trend of decrease.

The DMD modes associated with laminar separation-bubble (LSB) bursting appear at high Strouhal numbers (St ≈ 0.36–0.65), indicating rapid, transient events as the bubble collapses and reforms under adverse pressure gradients in Figure 32. Despite their intensity, these bursting modes carry only 0.34 %–2.51 % of the total kinetic energy, showing that bubble-burst events, while critical, represent a small fraction of the flow's energy budget. Their spatial structures are localized near the leading edge (x/c < 0.2) with alternating regions of positive and negative velocity fluctuations, capturing the instantaneous detachment and reattachment cycles of the separated shear layer (Raus, 2022). It is important to note that at higher k, as shown in Figure 32, the LSB bursts more abruptly as the adverse pressure gradient steepens so the corresponding bursting mode exhibits a sharper growth spike (larger St.) immediately prior to LEV formation due to amplified hysteresis effect of the flow (Dunne, 2016). Except for the pre-stall condition ($\alpha = 15°$), the modes associated with LSB bursting "decelerated" (Lower St.) as k is increased as shown through Figure 32 a, a-1, a-2.

Modal Frequency Spectrum Analysis:

Dynamic stall flows over a pitching airfoil exhibit DMD modes whose frequencies and growth/decay rates change systematically as the reduced frequency (*k*) and oscillation amplitude (peak angle of attack, AOA) increase. The onset of stall is highly sensitive to these motion parameters: the pitch amplitude, reduced frequency, and motion type all influence which flow instability triggers dynamic stall. At lower amplitudes and higher frequencies (e.g. 15° at k=0.3), the flow remains mostly attached or with a small leading-edge separation bubble, so the DMD spectrum is dominated by the imposed pitching frequency and its harmonics. These cases produce a few strong DMD modes at the driving frequency (Real(ω)=0, purely oscillatory) and its integer multiples, reflecting a near-periodic response of the flow to the motion. Such modes are neutrally stable ($Real(\omega) \approx 0$) or mildly decaying, indicating sustained periodic shedding or oscillation. This aligns with prior modal analyses showing the dominant flow structure oscillating at the airfoil's motion frequency (with several harmonics) when dynamic stall is mild. In essence, for gentle pitching, DMD captures primarily the coherent motion-induced vortex shedding which is phase-locked to the oscillation.

As the pitching amplitude and reduced time scale increase (e.g. *k* decreasing to 0.1, AOA up to 30°), the DMD spectra reveal new modes associated with the onset of deep dynamic stall. Physically, at higher AOA the laminar separation bubble (LSB) at the leading edge grows and eventually bursts, precipitating massive flow separation. In classical dynamic stall, this bubble burst is followed by a rapid roll-up of the shear layer and formation of a leading-edge vortex (LEV), (Visbal, 2018) often called the dynamic stall vortex (DSV) which sheds over the wing. As the pitching amplitude and reduced time scale increase (e.g. k decreasing to 0.1, AOA up to 30°)

(Miotto, 2022), the DMD spectra reveal new modes associated with the onset of deep dynamic stall. Physically, at higher AOA the laminar separation bubble (LSB) at the leading edge grows and eventually bursts, precipitating massive flow separation. In classical dynamic stall, this bubble burst is followed by a rapid roll-up of the shear layer and formation of a leading-edge vortex (LEV) – often called the dynamic stall vortex (DSV) – that shed over the wing. In the DMD spectrum, the LSB-burst mode can manifest as a highly decaying oscillatory mode (large negative Real(ω) indicating it is short-lived) at a moderately high imaginary frequency. These DMD mode positions thus shift with flow regime: higher-amplitude, slower pitching cases show more modes off the imaginary axis (decaying/growing), reflecting non-periodic transients, whereas lower-amplitude, fast pitching yields modes clustered near the imaginary axis (sustained oscillations). Meanwhile, as mentioned previously, once the LSB has burst and transitions to turbulence, its DMD mode decays more quickly (more negative real part) due to rapid turbulence production and shear-layer breakdown; and thereby we note that the corresponding bursting mode exhibits higher $|\lambda_j|$ values (Figure 28).

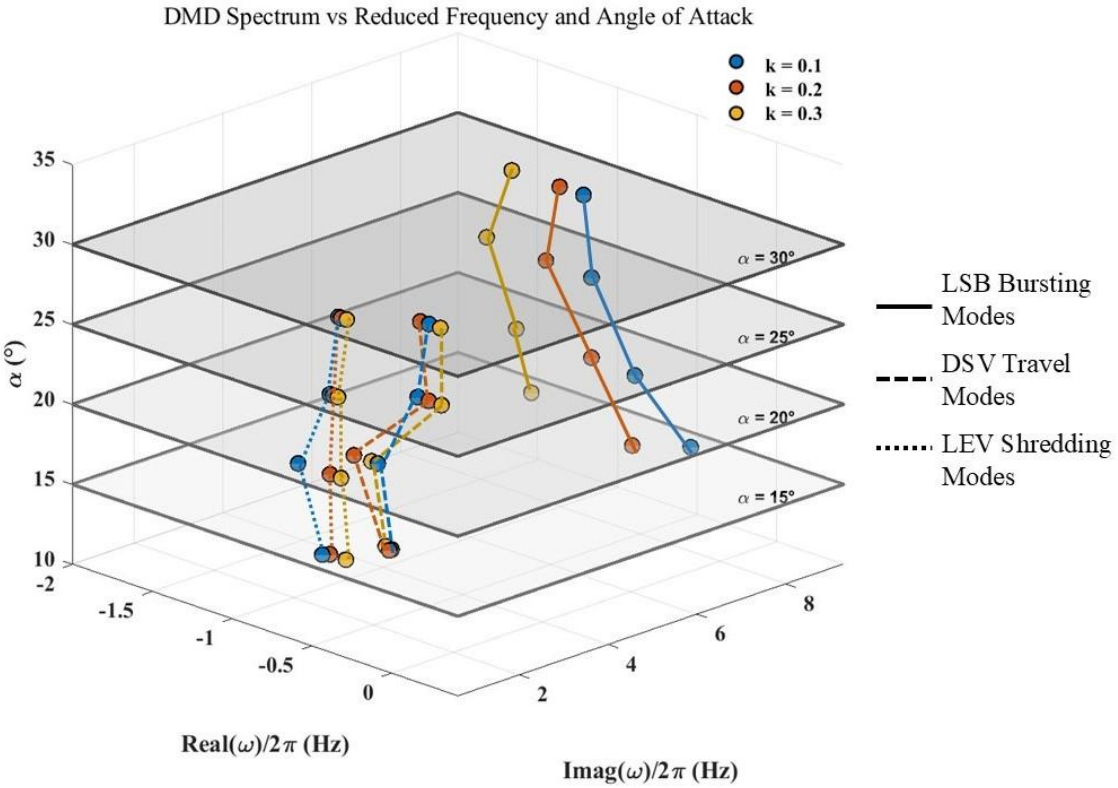

Figure 28 Spectrum modal analysis for flow events (LSB Bursting, DSV, LEV) undering varying reduced frequency (k) and Pitching Ampilitude (α)

Importantly, DMD indicates the stability of these flow structures. In Figure 28, the DSV (dynamic stall vortex) mode is often found to be unstable (positive growth rate) in deep stall cases ($\alpha = 25°, 30°$). This implies that as the airfoil pitches up, the DSV rapidly amplifies – it is a transient growth phenomenon rather than a steady oscillation. Indeed, Mohan et al. (2016) (Mohan, 2016) noted that the DMD mode associated with the DSV had a positive growth rate, signifying the vortex's sudden intensification during stall onset. As the vortex sheds and dissipates away, that mode's amplitude in the data then diminishes (hence DMD might capture it as growing then decaying within the cycle). Similarly, modes associated with trailing-edge or wake vortices shed after the DSV might appear at higher frequencies (related to small-scale vortices in the wake) and are usually decaying, indicating energy cascading to smaller scales.

Overall, as frequency k decreases and amplitude increases, the DMD eigenvalues migrate: new low-frequency modes with slight growth/decay emerge (capturing DSV formation and convection), and high-frequency decaying modes appear (capturing shear-layer and vortex shedding), complementing the base pitching-frequency mode. These trends match the known physics of dynamic stall. At low reduced frequency (slow pitch) and large amplitude, the flow has time to develop a pronounced LSB that eventually bursts (Honarmand, 2019), forming an energetic DSV. DMD picks up the LSB-burst and DSV-travel as separate modes. At higher k (fast pitch) or smaller amplitudes, the stall vortex either remains small or is entirely absent (attached flow with only mild separation), so the DMD spectrum simplifies to the forced motion harmonics. In summary, increasing unsteadiness and amplitude populate the DMD spectrum with additional modes representing key dynamic stall events: LSB bursting (a rapid, high-frequency breakaway of the leading-edge flow) (Kurtulus, 2015), DSV formation and convection (a dominant low-frequency, growing mode corresponding to the large vortex structure traveling along the wing), and subsequent LEV shedding or wake vortices (higher-frequency decaying modes as the vortex leaves the airfoil) (Schmid, 2010).

Reconstruction Error Analysis (DMD vs. mrDMD):

Comparing the reconstruction quality of standard DMD and multiresolution DMD (mrDMD) for the pitching airfoil cases reveals that *global* DMD achieves lower error in most conditions, in Figure 29, with mrDMD outperforming it only in the most challenging flow (slow, deep stall at k=0.1, α=30°). This result may seem counter-intuitive, since mrDMD is designed for complex, multi-scale data, but it highlights the importance of flow stationarity. Standard DMD considers the entire time series at once, finding a single set of modes (and linear eigenvalues)

that best fits all snapshots in a least-squares sense (Mohan, 2016). If the flow's dynamics are approximately periodic or dominated by a single frequency (as in cases with weaker stall), a global DMD expansion can efficiently capture the motion with fewer modes (e.g. the fundamental pitching frequency and its strongest harmonics) (Miotto, 2022). In fact, prior studies on periodic pitching have shown that the first few DMD modes often correspond to the fundamental and harmonic frequencies of the imposed motion (Kutz J. N., 2016). These global modes are spatially coherent over the entire cycle and can reconstruct the periodic flow physics with low error. mrDMD, on the other hand, performs DMD on sequential time blocks or at multiple resolutions, effectively isolating slow, medium, and fast dynamics in separate sets of modes. While this yields a rich and time-localized description of the flow, it can artificially introduce discontinuities or redundant modes if the flow was in fact dominated by a single coherent oscillation. In most of the pitching cases studied (except the most extreme one), the unsteady flow is largely phase-locked to the pitching motion and repeats each cycle, so a single global DMD basis is sufficient and perhaps optimal for reconstruction as shown in Figure 29 The multi-resolution approach, in those cases, may overfit or split the content unnecessarily to an extend where the approach introduced more reconstruction error than the standard DMD approach (e.g. approximately 7% more), resulting in a marginally lower reconstruction match with actual flow features.

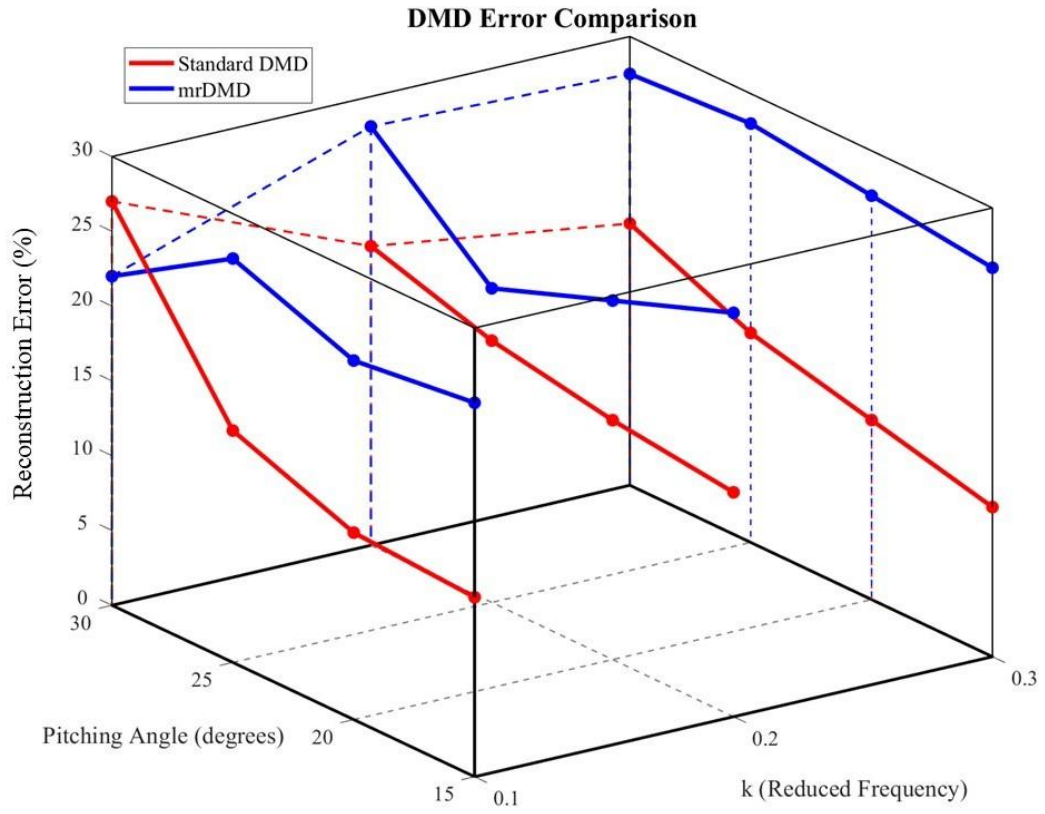

Figure 29 Error analysis using different Dynamic Mode Decomposition methods (DMD v.s. mrDMD)

In the deep dynamic stall case (k=0.1, α=30°), however, mrDMD shows its strength. Here the flow is highly non-stationary within each cycle: during the pitch-up, the leading-edge flow transitions from a laminar attached state to a separated shear layer with an LSB, then to a fully detached flow with a dynamic stall vortex, all in one half-cycle, followed by reattachment during pitch-down. These phases involve disparate time scales and flow structures that violate the assumption of a single linear oscillator. Indeed, the dynamic stall onset is an intermittent, transient event superposed on the base oscillation. A single set of global DMD modes struggles to capture this sequence of events with fixed frequencies – it tends to mix multiple phenomena into each mode. As noted by Miotto et al. (Miotto, 2022), the standard DMD modes in a dynamic stall flow can inadvertently combine pre-stall and post-stall features, because the

algorithm uses all snapshots together. For example, a DMD mode that highlights the leading-edge region might also include spurious influence from the later, fully stalled stages of the cycle if those snapshots are part of the input. This “smearing” of distinct temporal events into single modes can reduce reconstruction fidelity for highly transient data (Mohan, 2016). mrDMD mitigates this by analyzing shorter temporal windows and filtering by frequency content. In the k=0.1, 30° case, mrDMD can isolate the short-duration stall vortex formation in one low-frequency window and the remaining attached-flow oscillation in another, for instance. This yields modes that are more time-localized and tailored to each phase of the motion. Consequently, the mrDMD reconstruction better captures the sharp, brief lift breakdown and vortex shedding, improving accuracy (lower error) compared to global DMD. In essence, mrDMD succeeds here because it “resets” the modal basis when the flow’s character changes, whereas standard DMD tries to span a strongly changing flow with a fixed basis. Researchers have emphasized that for highly transient, multi-timescale problems, mrDMD provides a notable advantage: it can represent intermittent dynamics that standard DMD fails to capture. Our findings corroborate this – only in the deepest stall case (where events with widely varying time scales occur) does mrDMD’s adaptive decomposition yield a superior reconstruction. In all other cases, the flow dynamics are sufficiently uniform (dominated by the pitching frequency and its stable vortex shedding pattern) that a global DMD basis is already adequate and even preferable.

Chapter 6
Conclusion

The combined DES, POD, and DMD/mrDMD analysis offers a comprehensive picture of unsteady vortex dynamics during dynamic stall on a pitching NACA 0018 at Re = 160 000. POD identified that a handful of energetic modes (the leading-edge separation bubble, primary shear-layer vortices, and trailing-edge structures) capture over 90% of the flow's kinetic energy, confirming the low-dimensional nature of dynamic stall coherent structures. DMD further decomposed these dynamics into modes with associated Strouhal numbers (from 0.0351 to 0.451) and exponential growth/decay rates, isolating LSB bursting ($St = 0.451$, strongly decaying), LEV-shedding (weakly decaying at $St \approx 0.07$), and DSV convection ($St \approx 0.09 - 0.153$, slowly-decaying in pre/light-stall regime and positive growth in deep-stall regime) across the parametric space. As pitch amplitude increases and reduced frequency decreases, the DMD spectrum fills with transient modes off the imaginary axis, reflecting the transition from mild oscillatory separation to deep stall characterized by robust LEVs and trailing-edge vortices. Comparisons of standard DMD and mrDMD reconstructions revealed that a global DMD basis suffices for flows dominated by phase-locked shedding (small amplitude or high k), yielding lower velocity-norm error i.e. mrDMD methods yield 5% of more errors than most standard DMD cases. Only in the most non-stationary case (k = 0.1, 30°) does mrDMD's hierarchical, time-localized decomposition outperform DMD by isolating distinct phases of stall onset, vortex growth, and shedding. This highlights the importance of matching modal methods to flow non-stationarity when developing reduced-order models and active-control schemes.

Overall, this work bridges 2D and 3D perspectives, demonstrating that modal

decompositions not only reconstruct unsteady flow fields economically but also directly map to physical vortex events. The resulting low-order descriptions enable rapid prediction of unsteady loads and inform targeted stall-mitigation strategies—such as leading-edge morphing or timed actuations—to enhance performance and durability in rotary and flapping-wing application

Appendix A

Modal Shape from DMD and mrDMD analysis

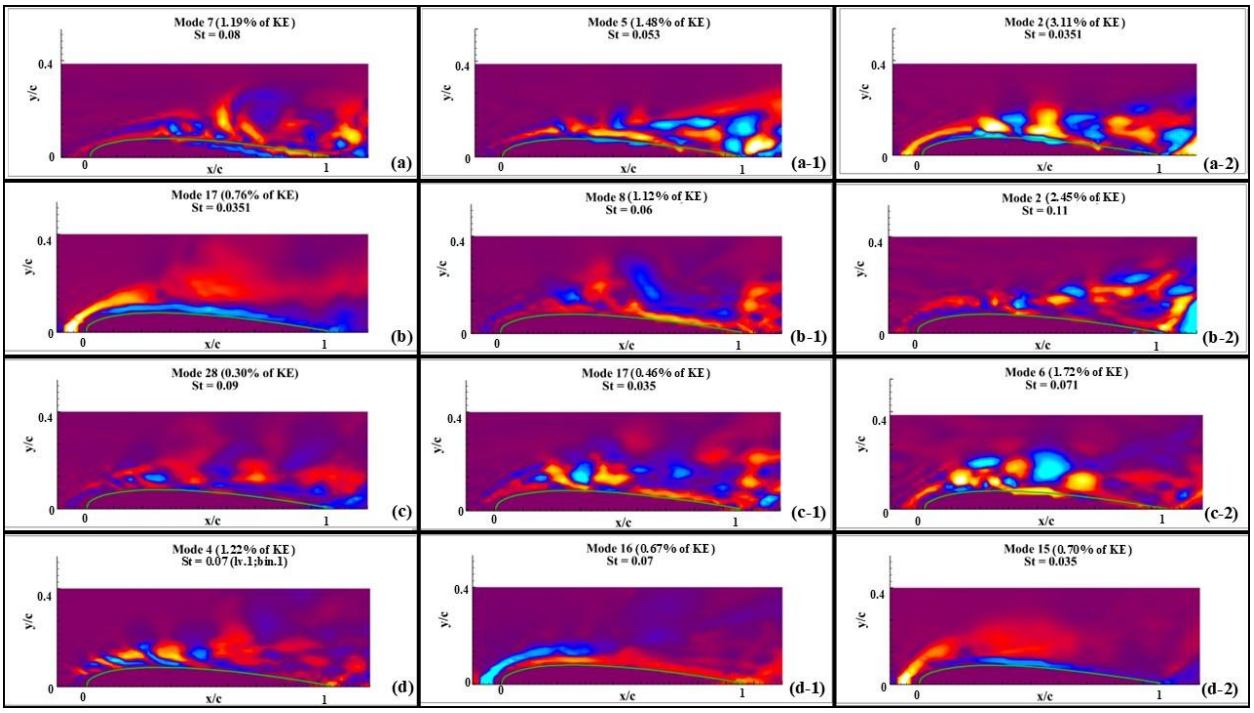

Figure 30 DMD modes for Leading-Edge Vortex (LEV) under varying pitching conditions

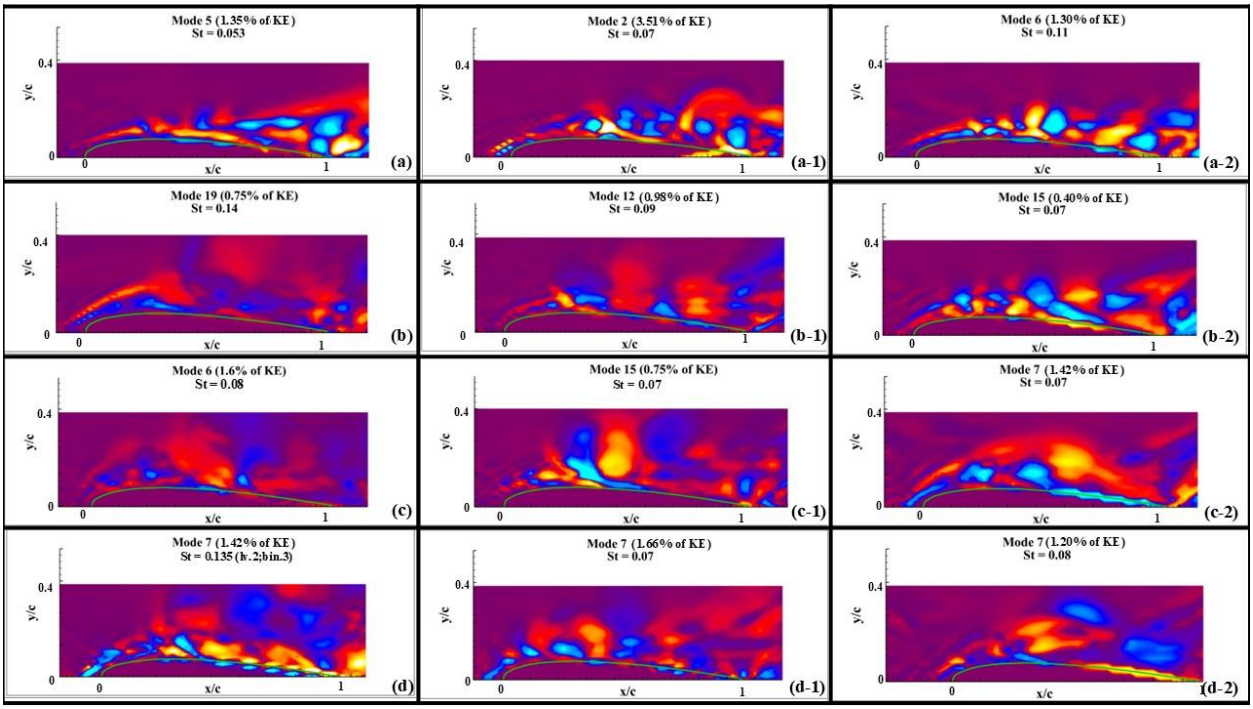

Figure 31 DMD modes for Dynamic Stall Vortex (DSV) under varying pitching conditions

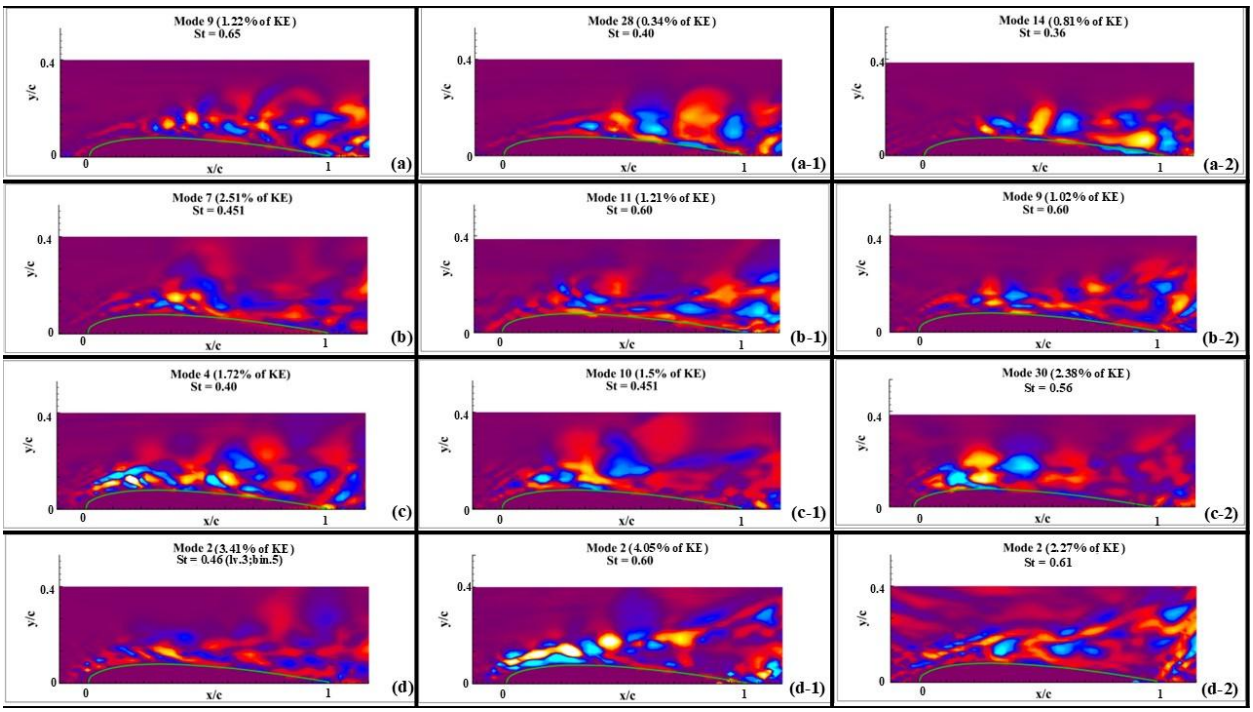

Figure 32 DMD modes for Laminar Separation Bubble (LSB) bursting under varying pitching conditions

Bibliography

Abbott, I. H. (2012). *Theory of wing sections: including a summary of airfoil data.* Courier Corporation.

Ahmad, M. a. (2023). Enhancing vertical axis wind turbine efficiency through leading edge tubercles: A multifaceted analysis. *Ocean Engineering*, 116206.

Akhtar, I. (2008). *Parallel simulations, reduced-order modeling, and feedback control of vortex shedding using fluidic actuators.* Virginia Tech.

Askham, T. a. (2018). Variable projection methods for an optimized dynamic mode decomposition. *SIAM Journal on Applied Dynamical Systems*, 380-416.

Badia, P. V. (2024). Dynamic stall on airfoils with leading-edge tubercles.

Batther, J. a. (2022). Numerical investigation of a pitching airfoil undergoing dynamic stall using Delayed Detached Eddy Simulations. *Computers & Fluids*, 105691.

Benton, S. a. (2019). The onset of dynamic stall at a high, transitional Reynolds number. *Journal of Fluid Mechanics*, 860--885.

Berkooz, G. a. (1993). The proper orthogonal decomposition in the analysis of turbulent flows. *Annual review of fluid mechanics*, 539-575.

Cai, C. a. (2022). Modeling of the compartmentalization effect induced by leading-edge tubercles. *Physics of Fluids*, 8.

Chatterjee, A. (2000). An introduction to the proper orthogonal decomposition. *Current science*, 808-817.

Drazin, P. (1970). Kelvin--Helmholtz instability of finite amplitude. *Journal of Fluid Mechanics*, 321-335.

Dunne, R. (2016). *Dynamic Stall on Vertical Axis Wind Turbines.* California Institute of Technology.

Dylewsky, D. a. (2019). Dynamic mode decomposition for multiscale nonlinear physics. *Physical Review E*, 063311.

Fish, F. E. (1995). Hydrodynamic design of the humpback whale flipper. *Journal of morphology*, 51-60.

Geng, F. a. (2018). Sensitivity analysis of airfoil aerodynamics during pitching motion at a Reynolds number of 1.35105. *Journal of Wind Engineering and Industrial Aerodynamics*, 315--332.

Guo, H. a. (2022). Numerical simulation of the flow around NACA0018 airfoil at high incidences by using RANS and DES methods. *Journal of Marine Science and Engineering*, 847.

Hand, B. a. (2017). Numerical simulation of a vertical axis wind turbine airfoil experiencing dynamic stall at high Reynolds numbers. *Computers & Fluids*, 12-30.

Hansen, K. L. (2012). *Effect of leading edge tubercles on airfoil performance.* University of Adelaide, School of Mechanical Engineering.

He, R. a. (2023). Effects of leading-edge tubercles on three-dimensional flapping foils. *Journal of Marine*

Science and Engineering, 1882.

Hemati, M. R. (2014). Dynamic mode decomposition for large and streaming datasets. *Physics of Fluids*, 111701.

Hill, N. a. (2009). Darrieus turbines: the physics of self-starting. *Proceedings of the Institution of Mechanical Engineers, Part A: Journal of Power and Energy*, 21-29.

Honarmand, M. a. (2019). Numerical simulation of a pitching airfoil under dynamic stall of low Reynolds number flow. *Journal of Aerospace Technology and Management*, e4819.

Hrynuk, J. T. (2020). The effects of leading-edge tubercles on dynamic stall. *Journal of Fluid Mechanics*, A5.

Hunt, J. C. (1991). Kolmogorov's contributions to the physical and geometrical understanding of small-scale turbulence and recent developments. *Proceedings of the Royal Society of London. Series A: Mathematical and Physical Sciences*, 183-210.

Jacobs, E. N. (1933). *The Characteristics of 78 related airfoil section from tests in the Variable-Density Wind Tunnel.* US Government Printing Office.

Kern, J. S. (2024). Direct numerical simulations of an airfoil undergoing dynamic stall at different background disturbance levels. *Journal of Fluid Mechanic*, Cambridge University Press.

Khalid, M. S. (2020). Modal decompositions of the kinematics of Crevalle Jack and the fluid--caudal fin interaction. *Bioinspiration & Biomimetics*, 016018.

Kolmogorov, A. N. (1941). The local structure of turbulence in incompressible viscous fluid for very large Reynolds. *Numbers. In Dokl. Akad. Nauk SSSR*, 301.

Kozelkov, A. a. (2016). Comparison of convective flux discretization schemes in detached-eddy simulation of turbulent flows on unstructured meshes. *Journal of Scientific Computing*, 176-191.

Kurtulus, D. F. (2015). On the unsteady behavior of the flow around NACA 0012 airfoil with steady external conditions at Re= 1000. *International journal of micro air vehicles*, 301-326.

Kutz, J. N. (2016). *Dynamic Mode Decomposition: Data-Driven Modeling of Complex Systems.* SIAM.

Kutz, J. N. (2016). Multiresolution dynamic mode decomposition. *SIAM Journal on Applied Dynamical Systems*, 713--735.

Laneville, A. a. (1986). *Dynamic stall: The case of the vertical axis wind turbine.*

Le Fouest, S. a. (2022). The dynamic stall dilemma for vertical-axis wind turbines. *Renewable Energy*, 505--520.

Lee, T. a. (2004). Investigation of flow over an oscillating airfoil. *Journal of Fluid Mechanics*, 313-341.

LeGresley, P. a. (2000). Airfoil design optimization using reduced order models based on proper orthogonal decomposition. In *Fluids 2000 conference and exhibit* (p. 2545).

Madsen, J. a. (2009). Investigation of grid resolution requirements for detached eddy simulation of flow

around thick airfoil sections. In *Proceedings of EWEC European Wind Energy Conference, Marseille.*

Mallik, W. a. (2020). Aerodynamic damping investigations of light dynamic stall on a pitching airfoil via modal analysis. *Journal of Fluids and Structures*, 103111.

McAlister, K. W. (1978). Dynamic stall experiments on the NACA 0012 airfoil.

McCroskey, W. J. (1981). *The Phenomenonof Dynamic Stall.*

MeloMelo De Sousa, J. a. (2013). Numerical study on the use of a sinusoidal leading edge for passive stall control at low Reynolds number. *51st AIAA aerospace sciences meeting including the new horizons forum and aerospace exposition*, 62.

Menon, K. a. (2021). Significance of the strain-dominated region around a vortex on induced aerodynamic loads. *Journal of Fluid Mechanics*, R3.

Menter, F. a. (2004). Adaptation of eddy-viscosity turbulence models to unsteady separated flow behind vehicles. *The aerodynamics of heavy vehicles: trucks, buses, and trains*, 339-352.

Miotto, R. a. (2022). Analysis of the onset and evolution of a dynamic stall vortex on a periodic plunging aerofoil. *Journal of Fluid Mechanics*, A24.

Mohan, A. T. (2016). Model reduction and analysis of deep dynamic stall on a plunging airfoil. *Computers & Fluids*, 1-19.

Ouro, P. a. (2018). Effect of blade cambering on dynamic stall in view of designing vertical axis turbines. *Journal of Fluids Engineering*, 061104.

Raus, D. a. (2022). Experimental study of the dynamic stall noise on an oscillating airfoil. *Journal of Sound and Vibration*, 117144.

Ribeiro, J. H. (2017). Identification of coherent structures in the flow past a NACA0012 airfoil via proper orthogonal decomposition. *Physics of Fluids*, 8.

Robertson, E. a. (2015). Validation of OpenFOAM numerical methods and turbulence models for incompressible bluff body flows. *Computers & Fluids*, 122-145.

Rowley, C. W. (2009). Spectral analysis of nonlinear flows. *Journal of Fluid Mechanics*, 115–127.

Schlichting, H. a. (2000). Boundary layer theory springer. *Eigth Revised and Enlarged Edition*.

Schmid, P. J. (2010). Dynamic mode decomposition of numerical and experimental data. *Journal of Fluid Mechanic*, 5-28.

Shur, M. L. (2008). A hybrid RANS-LES approach with delayed-DES and wall-modelled LES capabilities. *International journal of heat and fluid flow*, 1638--1649.

Spalart, P. R. (2009). Detached-eddy simulation. *Annual review of fluid mechanics*, 181--202.

Sreejith, B. a. (2020). Experimental and numerical study of laminar separation bubble formation on low Reynolds number airfoil with leading-edge tubercles. *Journal of the Brazilian Society of*

Mechanical Sciences and Engineering, 171.

Sudharsan, S. a. (2024). Criteria for dynamic stall onset and vortex shedding in low-Reynolds-number flows. *Journal of Fluid Mechanics*, A11.

Sun, Z. a. (2022). Accurate stall prediction for thick airfoil by Delayed Detached-Eddy Simulations. *Atmosphere*, MDPI.

Takemura, N. a. (2004). Low Frequency Oscillation of Laminar Separation Bubble Near Stall-Discussion on Turbulent Energy Production. *Japan Society of Aeronautical Space Sciences*, 114--120.

Tamaki, Y. a. (2023). Wall-resolved large-eddy simulation of near-stall airfoil flow at R ec= 10 7. *AIAA Journal*, 698--711.

Travin, A. a. (2000). Detached-eddy simulations past a circular cylinder. *Flow, turbulence and combustion*, 293--313.

Travin, A. K. (2006). Improvement of delayed detached-eddy simulation for LES with wall modelling. *ECCOMAS CFD 2006: Proceedings of the European Conference on Computational Fluid Dynamics, Egmond aan Zee, The Netherlands, September 5-8, 2006*.

Tsang, K. a. (2008). Dynamic stall behavior from unsteady force measurements. *Journal of Fluids and Structures*, 129--150.

Tu, J. H. (2013). *Dynamic mode decomposition: Theory and applications.* Princeton University.

Turner, J. M. (2020). Effect of spanwise domain size on direct numerical simulations of airfoil noise during flow separation and stall. *Physics of Fluids*, 6.

Verma, S. a. (2023). On the association of kinematics, spanwise instability and growth of secondary vortex structures in the wake of oscillating foils. *Proceedings of the Royal Society A*, 20230353.

Visbal, M. R. (2018). Analysis of dynamic stall on a pitching airfoil using high-fidelity large-eddy simulations. *AIAA Journal*, 46--63.

Wang, S. a. (2012). Turbulence modeling of deep dynamic stall at relatively low Reynolds number. *Journal of Fluids and Structures*, 191-209.

Wang, W. a. (2021). Study on dynamics of vortices in dynamic stall of a pitching airfoil using Lagrangian coherent structures. *Aerospace Science and Technology*, 106706.

Wang, Z. a. (2012). Proper orthogonal decomposition closure models for turbulent flows: a numerical comparison. *Computer Methods in Applied Mechanics and Engineering}*, 10--26.

Williams, D. R.-V. (2017). Modeling lift hysteresis on pitching airfoils with a modified Goman--Khrabrov model. *AIAA Journal*, 403--409.

Yang, C. a. (2022). Numerical study on cavitation--vortex--noise correlation mechanism and dynamic mode decomposition of a hydrofoil. *Physics of Fluids*, 12.

Zaman, K. a. (1988). A natural low frequency oscillation in the wake of an airfoil near stalling conditions. In *26th Aerospace Sciences Meeting* (p. 131).

Zhao, M. a. (2017). Numerical simulation of flow characteristics behind the aerodynamic performances on an airfoil with leading edge protuberances. *Engineering Applications of Computational Fluid Mechanics*, 193-209.

Zhao, M. a. (2021). Onset of dynamic stall of tubercled wings. *Physics of Fluids*, 8.

Zhao, M. a. (2023). Influences of leading-edge tubercle amplitude on airfoil flow field. *Journal of Thermal Science*, 1335--1344.